

Ab initio potential energy surfaces and trajectory studies of Aband photodissociation dynamics: $\text{CH}_3\text{I}^* \rightarrow \text{CH}_3 + \text{I}$ and $\text{CH}_3 + \text{I}^*$

Yoshiaki Amatatsu, Keiji Morokuma, and Satoshi Yabushita

Citation: *The Journal of Chemical Physics* **94**, 4858 (1991); doi: 10.1063/1.460571

View online: <http://dx.doi.org/10.1063/1.460571>

View Table of Contents: <http://scitation.aip.org/content/aip/journal/jcp/94/7?ver=pdfcov>

Published by the AIP Publishing

Articles you may be interested in

Full ninedimensional ab initio potential energy surfaces and trajectory studies of Aband photodissociation dynamics: $\text{CH}_3\text{I}^* \rightarrow \text{CH}_3 + \text{I}$, $\text{CH}_3 + \text{I}^*$, and $\text{CD}_3\text{I}^* \rightarrow \text{CD}_3 + \text{I}$, $\text{CD}_3 + \text{I}^*$

J. Chem. Phys. **104**, 9783 (1996); 10.1063/1.471758

Ab initio potential energy surfaces and trajectory studies of Aband photodissociation dynamics: $\text{ICN}^* \rightarrow \text{I} + \text{CN}$ and $\text{I}^* + \text{CN}$

J. Chem. Phys. **100**, 4894 (1994); 10.1063/1.467209

The photodissociation of dimethylnitrosamine studied by classical trajectories on a b i n i t i o potential energy surfaces

J. Chem. Phys. **94**, 5508 (1991); 10.1063/1.460486

Photodissociation dynamics of methylnitrite ($\text{CH}_3\text{O}-\text{NO}$) in the 300–400 nm range: An a b i n i t i o quantum mechanical study

J. Chem. Phys. **87**, 3522 (1987); 10.1063/1.452997

Classical trajectories using the full a b i n i t i o potential energy surface $\text{H}^- + \text{CH}_4 \rightarrow \text{CH}_4 + \text{H}^-$

J. Chem. Phys. **68**, 4406 (1978); 10.1063/1.435520



Ab initio potential energy surfaces and trajectory studies of A-band photodissociation dynamics: $\text{CH}_3\text{I}^* \rightarrow \text{CH}_3 + \text{I}$ and $\text{CH}_3 + \text{I}^*$

Yoshiaki Amatatsu and Keiji Morokuma
Institute for Molecular Science, Myodaiji, Okazaki 444, Japan

Satoshi Yabushita
Department of Chemistry, Faculty of Science, Hiroshima University, Hiroshima 730, Japan

(Received 24 October 1990; accepted 4 December 1990)

Ab initio contracted spin-orbit configuration interaction (SOC) calculations have been carried out to obtain potential energy surfaces of 3Q_0 and 1Q_1 excited states of methyl iodide as functions of all the geometrical parameters except for the three C-H stretches. The results are fitted to six-dimensional diabatic potential functions and their couplings. Classical trajectory calculations have been performed using these potential functions. The rotation of the CH_3 product in the I channel has been calculated to be perpendicular to the top axis and to have a peak at $N = 5$ and extend up to $N = 8$, whereas it is cold in the I^* channel, in good agreement with recent experiments. The CH_3 rotation is excited by the time trajectories arrive at the conical intersection region; this excitation is retained in the I-channel product because the 1Q_1 surface has a small bending force constant outside the conical intersection, whereas it is damped in the I^* channel because 3Q_0 still has a large bending force constant. The calculated distribution in the ν_2 umbrella vibrational mode of the CH_3 product is hot and has a peak at $\nu = 2$ for the I channel, and is cool for the I^* channel, in good agreement with recent experiments. This channel selectivity is due to the difference in the preferred structure of the CH_3 group outside the conical intersection region; while the 3Q_0 surface prefers a bent CH_3 until the $\text{CH}_3\text{-I}$ distance becomes very large, 1Q_1 wants a planar CH_3 . The location of conical intersection and the ground-excited energy difference there are in good agreement with those deduced from experiment if a dynamical effect is taken into account.

I. INTRODUCTION

The $A(n \rightarrow \sigma^*)$ band photodissociation of CH_3I had been extensively studied experimentally¹⁻¹⁴ and theoretically¹⁵⁻²² with a major focus on the ν_2 umbrella mode excitation of the CH_3 product. In this reaction (see Fig. 1), the photon is considered to take the CH_3I system to the 3Q_0 state, which crosses with the 1Q_1 state during the dissociation. The former state gives the products $\text{CH}_3 + \text{I}^*(^2P_{1/2})$ and the latter state $\text{CH}_3 + \text{I} (^2P_{3/2})$. However, in the last few years, several new experimental reports have appeared giving new insights in the detail of the dynamics. The recent experimental findings can be summarized as follows:

(i) The CH_3 product in the I channel is rotating around the axis perpendicular to the CH_3 top axis.²³⁻²⁶ The CH_3 product in the I^* channel has much less rotational excitation than in the I channel.^{23,25,26} This dynamics, therefore, can no longer be treated with a pseudolinear triatomic model as it used to be.

(ii) The vibrational distribution of the CH_3 product's ν_2 umbrella mode in the I channel has an inverse population, with a maximum around $\nu_2 = 2$,^{23,26-28} in qualitative agreement with earlier studies. On the other hand, the product in the I^* channel has primarily $\nu_2 = 0$.^{23,26,27,29-31}

(iii) There is some excitation of the ν_1 symmetric stretching mode in the CH_3 product.^{23,25,26,32,33}

(iv) The CH_3 umbrella motion takes place after the C-I bond is extended to some extent.³³ The polarization of the

emission changes from parallel to perpendicular in the curve crossing region.³⁴

However, individual results are different in detail from each other and we make a belief review on some important experimental reports. Powis and Black (PB)²⁵ have found in the photodissociation of CD_3I (as well as CH_3I)²⁴ that the CD_3 product in the I channel has relatively large population at $N = 8$ and has high rotational excitation up to $N = 14$ and that the product in the I^* channel has less excitation, with up to four angular momentum units. They have also found that

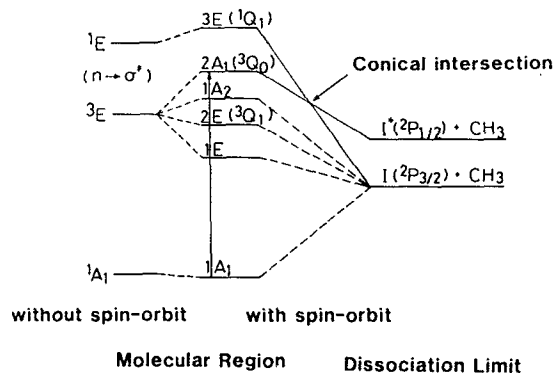


FIG. 1. A correlation diagram of the potential energy surfaces for C_{3v} dissociation without and with spin orbit.

the I^* channel product has a trend with $K \approx N$ and that I-channel product has $K \perp N$. Houston *et al.* have estimated the average CH_3 rotational excitation to be 125 cm^{-1} ,²³ which is lower than the PB estimation 208 cm^{-1} for CH_3 .²⁴ They have examined this difference and pointed out that PB results might be affected by the initial rotation of the parent CH_3I molecule. Chandler and co-workers have obtained results similar to Houston's; the rotational excitation extends only up to $N = 6$, and the average rotational energies around the axis perpendicular and parallel to the top axis are 106 and 8 cm^{-1} , respectively.²⁶

PB have shown that the I channel has an inverted CH_3 ν_2 vibrational population with its peak at $\nu_2 = 3$ and that the I^* channel has a peak at $\nu_2 = 2$ with the population ratio for $\nu_2 = 0, 1, 2$ of $1:1.1:2.0$,²⁸ which is very different from previous results, $1:4.4:14.6$ of Lee *et al.*⁸ Houston *et al.* have estimated the population ratio ($\nu_2 = 0$)/($\nu_2 = 2$) for CD_3 to be about 1.1 .²³ They have found that the I^* -channel product has primarily $\nu_2 = 0$. Chandler *et al.* have shown that the I/I^* ratio increases with the increasing vibrational quantum number.²⁶ Kanamori *et al.* have observed that the distribution in the ν_2 mode in the I^* channel monotonically decreases with the quantum number with the population ratio of $0.66:0.26:0.08:0.004$ for $\nu_2 = 0, 1, 2, 3$.³⁰ Hall *et al.* have found that the population ratio of the I^* -channel product is $4.3:2$ for $\nu_2 = 0, 1, 2$.³¹

The excitation in the ν_1 CH_3 symmetric stretching mode was in earlier days considered unlikely because the C–H bond distances of the parent CH_3I and the product CH_3 are almost identical and that the ν_1 mode has a much higher frequency than the ν_2 mode. PB have found that the ν_1 excitation occurs only in the CD_3 produced via the I channel, i.e., the ν_1 excitation has an isotope and channel specificity.²⁵ Houston *et al.* have found the ν_1 mode excitation for CH_3 species,²³ but they did not examine the channel specificity. Chandler *et al.* have observed that the I/I^* ratio of $\nu_1 = 1$ is > 2.0 , indicating that the I channel is more easily excited.²⁶ Kinsey and co-workers have observed the ν_1 mode excitation ($\nu_1 = 1$) by means of Raman emission spectroscopy.^{32,33}

Recent emission spectroscopy studies have made it possible to probe an evolution of the molecular dissociation on potential energy surfaces. Kinsey and co-workers have concluded that in the photodissociation of CH_3I , the C–I bond extension initially takes place to some extent before the subsequent umbrella motion sets in. Ref. 33. Lao *et al.* have observed that the polarization of the emission with lower quantum number in C–I stretch is parallel, but the polarization of the emission with the higher quantum number is perpendicular. From their observation, they have given a classical picture to the photodissociation through an electronic curve crossing, i.e., the amplitude of the molecular wave function gradually develops on the 1Q_1 repulsive surface as the molecule dissociates through a curve crossing.³⁴

On the theoretical side, Shapiro and Bersohn have treated the photodissociation dynamics of CH_3I as a linear triatomic system using empirical potential surfaces (denoted hereafter the SB surfaces) of the 3Q_0 and 1Q_1 states and adjusted their parameters to explain the dynamics such as

the ν_2 vibrational distribution of the CH_3 product, the branching ratio, and its wavelength dependence.^{15–17} The SB empirical surfaces have also been used for other dynamics studies.^{18,19} However, the SB surfaces, with only two degrees of freedom, the C–I stretch, and the CH_3 umbrella motion cannot handle the new experimental findings of CH_3 rotational excitation. Even for the CH_3 umbrella mode distribution, the SB surfaces give results (ν_2 hot in both channels) which agree with the old experiments,^{7–12} but disagree with new experimental findings mentioned above^{23,26,28,30,31} (ν_2 hot in the I channel, but cold in the I^* channel). Very recently Guo and Schatz have modified the SB surfaces (denoted hereafter the GS surfaces) to reproduce the new experimental findings.³⁵

We have recently calculated and reported preliminarily the general feature of the potential energy surfaces (PESs) of the two excited states for non- C_{3v} geometries of CH_3I , and have indicated that the bending near the $3E - 2A_1$ conical intersection can be the origin of the CH_3 rotational excitation.³⁶

The present study is an extended and thorough account of the study. We have calculated the potential energy surfaces of the excited states with an *ab initio* SOCI method and fitted them to analytical functions for six degrees of freedom (the C–I stretch, the CH_3 umbrella motion, the CH_3 deformation, and the CH_3 rock), i.e., all the degrees of freedom except for three C–H stretches. We have also performed classical trajectory calculations on these analytical potential functions. In Sec. II, we describe the method of calculation for obtaining the adiabatic energies, transformation from the adiabatic to the diabatic basis, and analytical fitting of diabatic energies. In Sec. III, we describe the method of classical trajectory calculation including the treatment of nonadiabatic transition based on a Landau–Zener model. In Sec. IV, we describe the global features of PESs, the results of classical trajectory calculations, and discussions on the origin of vibrational and rotational excitation. We also discuss the relationship between PES characteristics and dynamics and how the initial conditions affect the dynamics. Finally, we give our conclusions in Sec. V.

II. METHODS OF CALCULATION

A. Adiabatic energies

Ab initio spin-orbit configuration interaction (SOCI) calculations have been performed to obtain the potential energy surfaces. We have used a double-zeta-plus-polarization (DZP) basis set: the Huzinaga–Dunning double-zeta basis set for carbon and hydrogen atoms³⁷ and the Hay–Wadt relativistic effective core potential³⁸ and associated valence double-zeta basis functions augmented with a single *d*-polarization function on carbon ($\alpha_d = 0.75$) and iodine ($\alpha_d = 0.405$). The molecular orbitals have been determined by an open-shell restricted Hartree–Fock (RHF) calculation for the averaged $n \rightarrow \sigma^*$ excited states. SOCI calculations have been carried out with a modified COLUMBUS package,³⁹ using a one-electron spin-orbit Hamiltonian with an empirical nuclear charge.³⁶ In our previous calcula-

TABLE I. Comparison of excitation energies (in eV).^a

State	Contracted SOCI	Uncontracted SOCI
1A_1 ($1A_1$)	0.0 ^b	0.0 ^b
3Q_2 ($1E$)	4.455	4.457
3Q_1 ($2E$)	4.629	4.629
$^3Q_{0-}$ ($1A_2$)	4.984	4.991
$^3Q_{0+}$ ($2A_1$)	5.089	5.067
1Q_1 ($3E$)	5.450	5.448

^a At the experimental equilibrium geometry $R(\text{C-I}) = 2.132 \text{ \AA}$, $R(\text{C-H}) = 1.084 \text{ \AA}$, and $\langle \text{HCH} \rangle = 111.2^\circ$ with the C_{3v} symmetry (Ref. 41).

^b The total energy of the ground state is -51.008888 and -51.009699 hartree for contracted and uncontracted SOCI, respectively.

tions, we have used the uncontracted SOCI with about 5×10^5 configuration state functions for each of A' and A'' symmetry, arising from the single and double excitations out of the full valence ($\sigma, \sigma^*, e_x, e_y$)⁶ reference configurations (16 in A' and 12 in A''). In order to perform calculations at many points to obtain the analytical potential functions, we have used in the present paper a "contracted" SOCI method, which is similar to the method by Cohen *et al.*⁴⁰ First, a large-scale, spin-free CI calculation is performed to obtain the spin-free eigenstates and eigenvalues and then a small contracted SOCI matrix (12 dimensions in the C_1 double group symmetry, six (A') and six (A'') dimensions in C_s double group symmetry), which is composed of the diagonal matrix elements of the spin-free eigenstates obtained above and the off-diagonal matrix elements of spin-orbit interaction, is diagonalized and the adiabatic energies for each geometry are obtained. All the independent spin functions belonging to the lowest 1A_1 , 3E , 1E , and 3A_1 states of the spin-free CI are included in the contracted SOCI; the six A' independent functions included in the contracted SOCI are one 1A_1 , three 3E 's, one 1E , and one 3A_1 , and the six A'' functions are three 3E 's, one 1E , and two 3A_1 's. The inclusion of the high-lying 3A_1 states is essential to obtaining reasonable results in the contracted SOCI calculation. In Table I, we show an example of comparison of adiabatic energies between contracted and uncontracted SOCI calculations. The contracted SOCI results reproduce the uncontracted ones very well. The excitation energies of CH_3I at the experimental equilibrium geometry from the ground to the $n \rightarrow \sigma^*$ excited states 3Q_1 , $^3Q_{0-}$, $^3Q_{0+}$ (we refer to this state simply as 3Q_0 throughout the paper), and 1Q_1 are 4.63, 4.98, 5.09, and 5.45 eV, respectively, in reasonable agreement with the experimental broad A band centered around 260 nm (4.77 eV). The adiabatic energies at 170 points have been calculated, varying the C-I distance R , the umbrella angle α , the bending angle θ , the direction of the bend ϕ , and the projec-

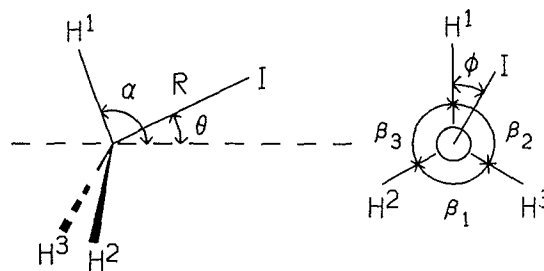


FIG. 2. The definition of internal coordinates. The broken line on the left is the axis for which the the umbrella angle is equal for all three CH's. The figure on the right is projection to the plane perpendicular to this axis. θ takes a value between 0 and π . ϕ is between 0 and 2π . β_i 's are redundant, satisfying $\beta_1 + \beta_2 + \beta_3 = 2\pi$.

tions of the three HCH angles to the plane perpendicular to the top axis β_i ($i = 1, 2, 3$) as defined in Fig. 2. The C-H bonds are fixed throughout the paper at $r_e = 1.084 \text{ \AA}$.⁴¹

B. Transformation from adiabatic to diabatic basis

In running a classical trajectory, we have to evaluate the adiabatic 3Q_0 and 1Q_1 potential energies and forces using analytical potential functions. However, it is hard to fit the adiabatic 3Q_0 and 1Q_1 energies to analytical functions because the character of each state changes with the geometry. Therefore, we transformed the adiabatic states to the diabatic states and fitted the latter to analytical functions. The transformation was carried out in the following way: Three adiabatic wave functions for each geometry can be written as in Eqs. (1)–(3):

$$^3\Psi = N_1(^3\psi_1 + \lambda_1^1\psi_1), \quad N_1 = 1/(1 + \lambda_1^2)^{1/2}, \quad (1)$$

$$^1\Psi_1 = N_2(^1\psi_2 + \lambda_2^2\psi_2), \quad N_2 = 1/(1 + \lambda_2^2)^{1/2}, \quad (2)$$

$$^1\Psi_2 = N_3(^1\psi_3 + \lambda_3^3\psi_3), \quad N_3 = 1/(1 + \lambda_3^2)^{1/2}. \quad (3)$$

$^3\Psi$, which is the adiabatic 3Q_0 wave function, mainly has a triplet $^3\psi_1$ character with a small singlet character $^1\psi_1$. $^1\Psi_1$, which is to have A' in C_s symmetry, is mainly a singlet $^1\psi_2$ with a small triplet $^3\psi_2$ character. $^1\Psi_2$, of A'' in C_s , mainly has another singlet $^1\psi_3$ character with a small triplet $^3\psi_3$ contribution. Three λ_i 's were determined by the uncontracted SOCI coefficients. For example, λ_1^2 is equal to the sum of the squares of the contracted SOCI coefficients of all the singlets (three singlets in C_1 , two for A' in C_s , and one for A'' in C_s in the SOCI). We transform these adiabatic wave functions [Eqs. (1)–(3)] using the matrix U defined in Eq. (4) into another set of wave functions in Eq. (5).

$$U = \begin{pmatrix} 1 & 0 & 0 \\ 0 & \cos A & \sin A \\ 0 & -\sin A & \cos A \end{pmatrix} \begin{pmatrix} \cos B & \sin B & 0 \\ -\sin B & \cos B & 0 \\ 0 & 0 & 1 \end{pmatrix} \begin{pmatrix} \cos C & 0 & \sin C \\ 0 & 1 & 0 \\ -\sin C & 0 & \cos C \end{pmatrix}, \quad (4)$$

$$\begin{pmatrix} {}^3\Phi_1 \\ {}^1\Phi_2 \\ {}^1\Phi_3 \end{pmatrix} = \begin{pmatrix} a_{11} & a_{12} & a_{13} \\ a_{21} & a_{22} & a_{23} \\ a_{31} & a_{32} & a_{33} \end{pmatrix} \begin{pmatrix} {}^3\Psi \\ {}^1\Psi_1 \\ {}^1\Psi_2 \end{pmatrix} = U \begin{pmatrix} {}^3\Psi \\ {}^1\Psi_1 \\ {}^1\Psi_2 \end{pmatrix}, \quad (5)$$

$${}^3\Phi_1 = (a_{11}N_1^3\psi_1 + a_{12}N_2^3\psi_2 + a_{13}N_3^3\psi_3) + (a_{11}\lambda_1N_1^1\psi_1 + a_{12}N_2^1\psi_2 + a_{13}N_3^1\psi_3), \quad (6)$$

$${}^1\Phi_2 = (a_{21}\lambda_1N_1^1\psi_1 + a_{22}N_2^1\psi_2 + a_{23}N_3^1\psi_3) + (a_{21}N_1^3\psi_1 + a_{22}\lambda_2N_2^3\psi_2 + a_{23}\lambda_3N_3^3\psi_3), \quad (7)$$

$${}^1\Phi_3 = (a_{31}\lambda_1N_1^1\psi_1 + a_{32}N_2^1\psi_2 + a_{33}N_3^1\psi_3) + (a_{31}N_1^3\psi_1 + a_{32}\lambda_2N_2^3\psi_2 + a_{33}\lambda_3N_3^3\psi_3). \quad (8)$$

The angle A , for instance, in Eq. (4) determines the transformation between the two adiabatic 1Q_1 states ${}^1\Psi_1$ and ${}^1\Psi_2$. The following function $f(A, B, C)$ gives the sum of weights of minor spin components over the three states:

$$\begin{aligned} f(A, B, C) &= \int [(a_{11}\lambda_1N_1^1\psi_1 + a_{12}N_2^1\psi_2 + a_{13}N_3^1\psi_3)^2 + (a_{21}N_1^3\psi_1 + a_{22}\lambda_2N_2^3\psi_2 + a_{23}\lambda_3N_3^3\psi_3)^2 \\ &\quad + (a_{31}N_1^3\psi_1 + a_{32}\lambda_2N_2^3\psi_2 + a_{33}\lambda_3N_3^3\psi_3)^2] d\tau \\ &= a_{11}^2N_1^2\lambda_1^2 + a_{12}^2N_2^2 + a_{13}^2N_3^2 + a_{21}^2N_1^2 + a_{22}^2N_2^2\lambda_2^2 + a_{23}^2N_3^2\lambda_3^2 + a_{31}^2N_1^2 + a_{32}^2N_2^2\lambda_2^2 + a_{33}^2N_3^2\lambda_3^2 \\ &\quad + 2a_{11}a_{12}N_1N_2\lambda_1\langle {}^1\psi_1 | {}^1\psi_2 \rangle + a_{11}a_{13}N_1N_3\lambda_1\langle {}^1\psi_1 | {}^1\psi_3 \rangle + a_{12}a_{13}N_2N_3\langle {}^1\psi_2 | {}^1\psi_3 \rangle \\ &\quad + a_{21}a_{22}N_1N_2\lambda_2\langle {}^3\psi_1 | {}^3\psi_2 \rangle + a_{21}a_{23}N_1N_3\lambda_3\langle {}^3\psi_1 | {}^3\psi_3 \rangle \\ &\quad + a_{22}a_{23}N_2N_3\lambda_2\lambda_3\langle {}^3\psi_2 | {}^3\psi_3 \rangle + a_{31}a_{32}N_1N_2\lambda_2\langle {}^3\psi_1 | {}^3\psi_2 \rangle \\ &\quad + a_{31}a_{33}N_1N_3\lambda_3\langle {}^3\psi_1 | {}^3\psi_3 \rangle + a_{32}a_{33}N_2N_3\lambda_2\lambda_3\langle {}^3\psi_2 | {}^3\psi_3 \rangle. \end{aligned} \quad (9)$$

Though we cannot eliminate the minor spin components completely, i.e., $f(A, B, C) = 0$, we can minimize it as far as possible by choosing A , B , and C to satisfy Eq. (10)

$$\partial f / \partial A = \partial f / \partial B = \partial f / \partial C = 0. \quad (10)$$

Using U thus determined, we transform with Eq. (11) three adiabatic energies $E({}^1Q_1)$, $E({}^1Q_2)$, and $E({}^3Q_0)$ to six diabatic matrix elements at each geometry

$$\begin{pmatrix} V_3 & V_{13} & V_{23} \\ V_{13} & V_1 & V_{12} \\ V_{23} & V_{12} & V_2 \end{pmatrix} = U \begin{bmatrix} E({}^3Q_0) & 0 & 0 \\ 0 & E({}^1Q_1) & 0 \\ 0 & 0 & E({}^1Q_2) \end{bmatrix} U^{-1}, \quad (11)$$

where $V_{ij} = \int \Phi_i^* H \Phi_j d\tau$ and $V_i = V_{ii}$. We note that the order of the operations in Eq. (4) is arbitrary. Though a different order of the operations gives a difference in a set of angles A , B , C , which satisfies Eq. (10), it does not change the transformation matrix U in Eq. (4) and, therefore, six diabatic matrix elements on the left-hand side of Eq. (11) are independent of the order of the operations.

C. Analytical fitting of diabatic potential terms

We have fitted the six diabatic matrix elements to analytical functions with respect to seven internal coordinates. The C_{3v} geometries are determined only by R and α , with all the other parameters to be zero. Changes of the other parameters from zero lower the symmetry from C_{3v} to C_s or C_1 .

First, we describe the three diagonal terms. In the present system, there is an energetic and symmetry hierarchy with respect to the internal coordinates. The diagonal terms change within 0.1 hartree with respect to R , within 0.01 hartree with respect to α , and within 0.001 hartree with respect to the other parameters θ , ϕ , and β_i ($i = 1, 2, 3$) in the region probed in the dynamics. We have also found that the diabatic terms obey a good additivity rule among the θ , ϕ , and β_i 's contributions. Furthermore, we have to consider the requirement that the adiabatic 3Q_0 and 1Q_1 energies are unchanged by permutation among the three hydrogens, which relates the internal parameters ϕ and β_i . A detailed discussion on this requirement is given in Appendix. This requirement leads us to two restrictions about the fitting forms of the diabatic potential functions; there should be a coupling between ϕ and β_i and there should be some relationships among the fitting forms of six diagonal and off-diagonal terms. Based on the above discussion, we first fitted the diagonal elements at the C_{3v} geometries to analytical functions of R and α . Then, we fitted the differences between the C_{3v} and the non- C_{3v} values; this procedure ensures that the relatively small energy dependence in θ , ϕ , and β_i is properly reproduced in the fitted functions. In the non- C_{3v} fitting, the θ , ϕ , and β_i 's contributions have been fitted independently in view of the additivity mentioned above. The actual forms of fitting functions are given below for the two diabatic singlets [Eqs. (12) and (13), corresponding to the A' and the A'' states in the C_s symmetry, respectively] and for the diabatic triplet state [Eq. (14)]

$$\begin{aligned} V_1 &= (A_0 + A_1 \Delta R) \exp(-A_5 \Delta R) + V_{\text{CH}_3} \\ &\quad + \{A_2 \sin^2 \theta + A_3 [1 + X(\phi, \beta_2, \beta_3, \zeta)] \sin \theta\} \\ &\quad \times \exp(-A_5 \Delta R) + A_4 S_a \exp(-A_6 \Delta R), \end{aligned} \quad (12)$$

$$V_2 = (A_0 + A_1 \Delta R) \exp(-A_5 \Delta R) + V_{\text{CH}_3} \\ + \{A_2 \sin^2 \theta + A_3 [1 - X(\phi, \beta_2, \beta_3, \xi)] \sin \theta\} \\ \times \exp(-A_5 \Delta R) - A_4 S_a \exp(-A_6 \Delta R), \quad (13)$$

$$V_3 = (B_0 + B_1 \Delta R) \exp(-B_3 \Delta R) + V_{\text{CH}_3} + \Delta E_I \\ + B_2 \sin^2 \theta \exp(-B_3 \Delta R). \quad (14)$$

The variables used, in addition to θ , are

$$\Delta R = R - R_e, \quad \Delta \alpha = \alpha - \pi/2, \quad \Delta \beta_i = \beta_i - 2\pi/3 \\ (i = 1, 2, 3),$$

$$S_a = 1/\sqrt{6}(2\Delta\beta_1 - \Delta\beta_2 - \Delta\beta_3),$$

$$S_b = 1/\sqrt{2}(\Delta\beta_2 - \Delta\beta_3),$$

$$X(\phi, \beta_2, \beta_3, \xi) = \{\cos(3\phi + \xi) + \cos[3(\phi + \beta_3) + \xi] \\ + \cos[3(\phi - \beta_2) + \xi]\}/3, \\ \times \tan \xi = S_b/S_a,$$

and r_e and R_e are the equilibrium C-H and C-I distances. The coefficients A_0 to A_6 , and B_0 to B_3 , represented in general by Z_i , are the following functions of $\Delta\alpha$:

$$Z_i = Z_{i0} + Z_{i1} \sin \Delta\alpha + Z_{i2} \sin^2 \Delta\alpha, \quad (15)$$

V_{CH_3} is the term which reproduces the CH_3 force field in the dissociation limit, and we used Spiko and Bunker's empirical CH_3 force field.⁴²

$$V_{\text{CH}_3} = G_2 (r_e \sin \Delta\alpha)^2 + G_4 (r_e \sin \Delta\alpha)^4 \\ + G_6 (r_e \sin \Delta\alpha)^6 + H_2/2(S_a^2 + S_b^2). \quad (16)$$

$\Delta E_I = 0.034\,646$ hartree in Eq. (14) is the energy difference between the ground ($^2P_{3/2}$) and the excited ($^2P_{1/2}$) states of the iodine atom.

The first lines on the right-hand side of Eqs. (12) and (13), which depend only on R and α and are the largest contributions to V_1 and V_2 , are the same since they represent

the C_{3v} symmetry where V_1 and V_2 are degenerate. The second lines, relating to the direction of bending of the I atom, are different from each other, though they share the common exponential factor A_5 due to the energetic hierarchy and the convenience. The potential curves with respect to $\sin \theta$ all fit well to a parabola. With respect to ϕ , all the diagonal terms have a threefold symmetry, with the energy minimum at $\phi = 0^\circ$ for V_1 and $\phi = 180^\circ$ for V_2 when the CH_3 group has a local C_{3v} symmetry. The second lines represent these angular dependencies. The third lines in Eqs. (12) and (13), relating to the CH_3 deformation, differ only in sign between Eqs. (12) and (13). The first term on the third line, which was determined in the C_s symmetry, is linear with respect to $\Delta\beta_i$'s. The coefficients of diagonal terms are listed in Table II.

Next, we describe the fitting forms of the off-diagonal elements, which are shown in Eqs. (17), (18), and (19):

$$V_{13} = D_1 X(\phi, \beta_2, \beta_3, \xi) \sin \theta / [(R - D_2)^2 + D_3^2] \\ + D_4 S_a / [(R - D_5)^2 + D_6^2], \quad (17)$$

$$V_{23} = -D_1 Y(\phi, \beta_2, \beta_3, \xi) \sin \theta / [(R - D_2)^2 + D_3^2] \\ - D_4 S_b / [(R - D_5)^2 + D_6^2], \quad (18)$$

$$V_{12} = A_3 Y(\phi, \beta_2, \beta_3, \xi) \sin \theta \exp(-A_5 \Delta R) \\ + A_4 S_b \exp(-A_6 \Delta R), \quad (19)$$

where

$$Y(\phi, \beta_2, \beta_3, \xi) \\ = \{\sin(3\phi + \xi) + \sin[3(\phi + \beta_3) + \xi] \\ + \sin[3(\phi - \beta_2) + \xi]\}/3.$$

These off-diagonal elements are all zero within the C_{3v} symmetry. Since the diabatic states $^1\Phi_1$ and $^1\Phi_2$ belong to A' and A'' in the C_s symmetry, respectively, V_{23} is 0 in the C_s sym-

TABLE II. Potential function parameters: coefficients of diagonal terms.^{a,b}

	X_{i0}	X_{i1}	X_{i2}
A_0	0.140 181	-0.124 719	0.043 310
A_1	0.088 560	-0.048 580	-0.163 996
A_2	0.141 458	-0.384 253	0.339 277
A_3	-0.003 932	0.002 520	-0.000 993
A_4	-0.002 909	0.005 382	-0.006 503
A_5	1.992 96	-0.127 307	-1.410 67
A_6	0.810 876	2.410 01	0.0
B_0	0.099 686	-0.153 511	0.064 085
B_1	-0.068 734	0.068 596	-0.059 619
B_2	0.099 668	-0.181 578	0.089 516
B_3	0.874 084	-0.337 881	2.610 930
CH_3 force field			
G_2	0.012 319	G_4	0.026 889
H_2	0.096 837	G_6	-0.000 889

^aIn units of a.u.

^bConstants are $R_e = 4.028\,89$ a.u. and $r_e = 2.0484$ a.u.

metry, whereas V_{13} is nonzero even in C_s . The singlet–triplet coupling terms V_{13} and V_{23} have been found to be reproduced well by Lorentzian functions which have the maximum with respect to R near the conical intersection. The off-diagonal term V_{12} between the two singlet states has been found to fit well to the function relating to the ϕ and β_i 's parts of the diagonal term V_1 (or V_2), which satisfies the second requirement as pointed out before. The coefficients D_1 to D_6 in Eqs. (17) and (18) are also functions of α , as are given in Eq. (15). The coefficient sets of the off-diagonal terms are listed in Table III.

In Fig. 3, the adiabatic energies of the *ab initio* SOCI calculation are compared with those from the fitted analytical potential functions. The standard deviations of the fit were 0.0933, 0.0033, and 0.0036 eV for Figs. 3(a), 3(b), and 3(c), respectively. Note the difference in energy scale of Fig. 3(a) from that of Figs. 3(b) and 3(c). For each hierarchy of variables, the *ab initio* energies are well reproduced by the analytical functions. We use thus obtained analytical potential energy functions without modification in classical surface hopping trajectory calculation.

III. CLASSICAL TRAJECTORY CALCULATIONS

A. Initial conditions

Since parent molecules CH_3I in most relevant experiments are cooled in supersonic expansion, they are considered to be at the vibrational ground state. The rotation of the entire molecule or its coupling with vibration has not been considered. Therefore, the normal mode description can be used for initial conditions of classical trajectory calculations.⁴³ First, nine normal mode coordinates of CH_3I were determined according to Eqs. (20) and (21):

$$Q_k(t) = Q_k^0 \cos(\lambda_k^{1/2} t + \delta_k) \quad (k = 1, 2, \dots, 9), \quad (20)$$

$$Q_k^0 = (2\epsilon_k/\lambda_k)^{1/2}, \quad (21)$$

$$\epsilon_k = \lambda_k^{1/2}(v_k + 1/2), \quad (22)$$

$$\delta_k = 2\pi\xi_k. \quad (23)$$

λ_k 's were obtained by diagonalizing the force constant matrix of the ground state of CH_3I (Table IV), which was determined by the contracted SOCI calculations described in Sec. II A. The calculated frequencies well reproduced the observed ones.⁴⁴ ϵ_k is the energy of mode k with a vibration-

TABLE III. Potential function parameters: coefficients of off-diagonal terms.*

	X_{D_1}	X_{D_2}	X_{D_3}
D_1	0.004 618	−0.011 405	0.011 226
D_2	4.223 43	0.437 838	0.0
D_3	0.662 089	0.490 741	0.0
D_4	−0.000 436	0.001 009	−0.001 683
D_5	4.300 19	0.316 343	0.0
D_6	0.941 249	0.027 870	0.0

*In units of a.u.

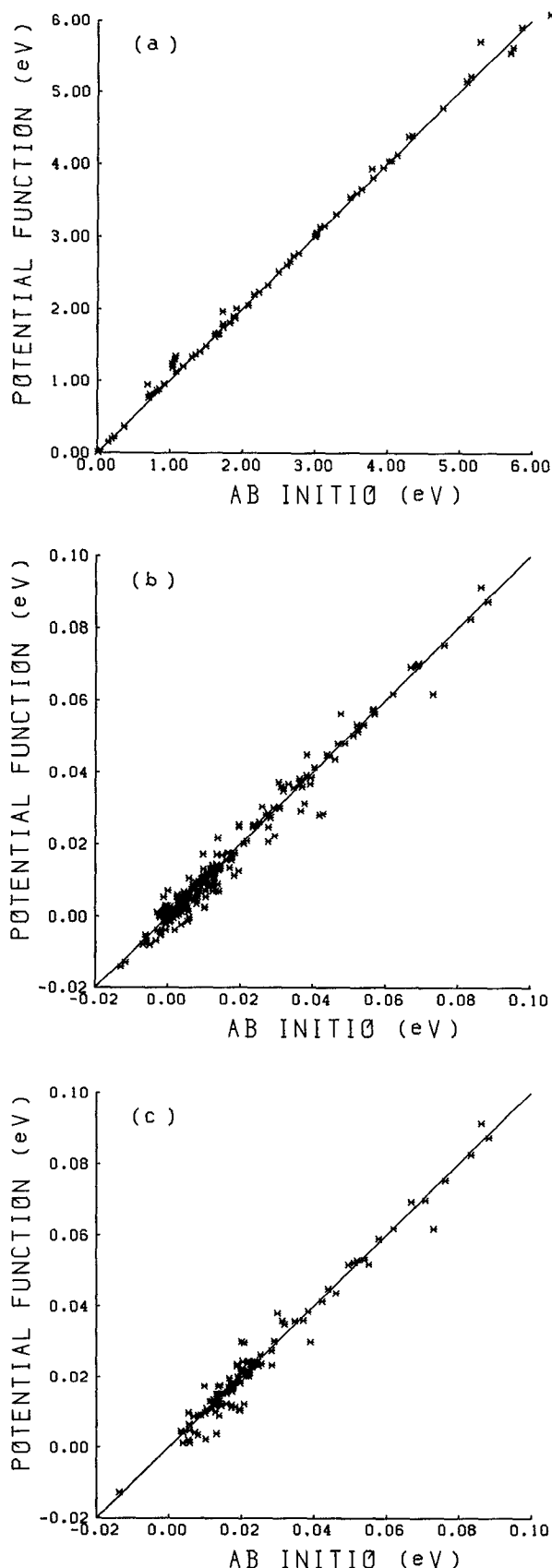


FIG. 3. A comparison of the adiabatic energies between *ab initio* calculations vs analytical functions fitted. (a) The energy at the C_{3v} geometry; (b) the energy difference between the C_{3v} geometry and the non- C_{3v} geometry with respect to θ and ϕ ; and (c) the energy difference between the C_{3v} geometry and the non- C_{3v} geometry with respect to β_i 's.

TABLE IV. Calculated vibrational frequencies (in cm^{-1}) and their L matrix

a_1 symmetry	3105.2 (2933) ^a	1346.3 (1252)	562.4 (533)
S_1	-0.997 451	-0.002 227	-0.016 053
S_2	-0.051 969	-0.982 293	-0.139 558
S_3	0.048 904	0.187 339	-0.990 084
e symmetry	3254.2 (3060)	1541.0 (1436)	891.4 (882)
S_4	-0.997 451	-0.002 227	-0.016 053
S_5	-0.051 969	-0.982 293	-0.139 558
S_6	0.048 904	0.187 339	-0.990 084
Definition of Symmetry Coordinates ^b			
a_1 CH_3 s str.	$S_1 = 1/\sqrt{3}(\Delta r_1 + \Delta r_2 + \Delta r_3)$		
CH_3 s def.	$S_2 = 1/\sqrt{6}(\Delta \alpha_1 + \Delta \alpha_2 + \Delta \alpha_3 - \Delta \gamma_1 - \Delta \gamma_2 - \Delta \gamma_3)$		
CI str.	$S_3 = \Delta R$		
e CH_3 d str.	$S_{4a} = 1/\sqrt{6}(2\Delta r_1 - \Delta r_2 - \Delta r_3)$		
	$S_{4b} = 1/\sqrt{2}(\Delta r_2 - \Delta r_3)$		
CH_3 d def.	$S_{5a} = 1/\sqrt{6}(2\Delta \gamma_1 - \Delta \gamma_2 - \Delta \gamma_3)$		
	$S_{5b} = 1/\sqrt{2}(\Delta \gamma_2 - \Delta \gamma_3)$		
CH_3 d rock.	$S_{6a} = 1/\sqrt{6}(2\Delta \alpha_1 - \Delta \alpha_2 - \Delta \alpha_3)$		
	$S_{6b} = 1/\sqrt{2}(\Delta \alpha_2 - \Delta \alpha_3)$		

^aThe numbers in the parentheses are observed frequencies from Ref. 43.

^b R is the distance between C and I atoms, r_i is the distance between C and H' atoms, α_i is the angle of $\text{H}'\text{CI}$, and γ_i is the angle of $\text{H}'\text{CH}^k$; $(i,j,k) = (1,2,3), (2,3,1), (3,1,2)$.

al quantum number v_k in Eq. (22) (in the present trajectory calculation, all v_k 's were set to 0 except for the cases specified explicitly in Sec. IV D). The phase factor of vibration δ_k was calculated according to Eq. (23), where ξ_k is a random number uniformly distributed between 0 and 1.

Normal coordinates and conjugate momenta were transformed into Cartesian coordinates and conjugate momenta, which were used as the initial conditions of 500 trajectories on the excited states.

B. Condition of integration

In our main calculation, we started each trajectory on the 3Q_0 adiabatic surface. A discussion on the trajectories starting on the 1Q_1 surface will be given in a discussion. This is based on the experimental finding that the A band is dominated by the transition from the ground to the 3Q_0 state. Integration of the Hamilton equation of motion on the adiabatic surfaces was carried out by the Runge-Kutta method. In the present calculation, three C-H bond distances were fixed at r_e . This was done by giving very large force constants with respect to three C-H stretches. The time step used for integration was 0.1 fs. When the absolute value of the difference between a triplet (V_3) and a singlet (V_1 or V_2) diabatic term was less than 10^{-3} a.u., the time step was reduced to 0.01 fs in order to determine the timing of nonadiabatic transitions accurately.

C. Treatment of nonadiabatic transition

As a trajectory evolves in time, the 3Q_0 diabatic surface, correlating to the $\text{CH}_3 + \text{I}^*$ dissociation limit, must cross the 1Q_1 surface, correlating to the $\text{CH}_3 + \text{I}$ limit. In our trajectory calculation, the nonadiabatic transition between the two surfaces was treated as follows: When the energy difference between one of the diabatic singlets and the triplet $V_1 - V_3$ or $V_2 - V_3$ changed the sign from positive to negative, which occurred only once for $V_1 - V_3$ and $V_2 - V_3$, respectively, in each trajectory, the transition probability P was calculated based on the Landau-Zener model⁴⁵ according to Eq. (24)

$$P = 1 - \exp(-2\pi V_{ij}^2/v_1 \Delta F_{ij}) \quad (i,j) = (1,2) \text{ or } (1,3)$$

$$\Delta F_{ij} = |F_i - F_j|. \quad (24)$$

F_i and v_1 are the diabatic force and the velocity of this trajectory to the direction perpendicular to the crossing seam. Whether the transition is allowed or not was determined by the Monte Carlo method;⁴⁶ if the diabatic transition probability P is greater than a random number ξ uniformly distributed between 0 and 1, the transition is allowed and the trajectory is hopped onto the diabatic singlet surface, correlating to $\text{CH}_3 + \text{I}$; otherwise, the trajectory remains on its present diabatic surface, which correlates $\text{CH}_3 + \text{I}^*$ in the dissociation limit. In the latter case, the trajectory crosses the other singlet surface within several time steps after the first crossing. At this point, the transition probability was calculated again and it was determined whether the surface hopping takes place here or not. In any case, the actual trajectory calculation was carried out on the adiabatic PES's and the correction to the momentum perpendicular to the seam was made in order to conserve the total energy of the trajectory.

D. Analysis of trajectories

When the distance between the CH_3 center of mass and the I atom was greater than 20.0 a.u., the trajectory was stopped and the vibrational quantum number v_2 of the CH_3 v_2 mode and the rotational quantum number were calculated.

The potential energy ϵ_{pot} contributing to the CH_3 v_2 umbrella mode depends only on the inversion angle α , and the kinetic energy ϵ_{kin} of the v_2 mode is calculated by the CH_3 internal velocity components perpendicular to $r_{\text{CH}i}$ ($i = 1, 2, 3$). The vibrational quantum number v_2 was calculated from the sum of potential and kinetic energies according to Eq. (25), where $\tilde{\nu}_2$ is the fundamental frequency of the umbrella mode, and was rounded off to an integer

$$\epsilon_{\text{tot}} = \epsilon_{\text{pot}} + \epsilon_{\text{kin}} = \tilde{\nu}_2 (v_2 + 1/2). \quad (25)$$

The CH_3 rotational quantum number N was calculated by taking the rotational angular momentum $L_{\text{CH}_3}^{\text{rot}}$ around the CH_3 center of mass and was rounded off to an integer

$$L_{\text{CH}_3}^{\text{rot}} = \sum_{i=1}^3 m_i (\mathbf{r}_i - \mathbf{r}_{\text{c.m.}}) \times (\dot{\mathbf{r}}_i - \dot{\mathbf{r}}_{\text{c.m.}}),$$

$$N = |L_{\text{CH}_3}^{\text{rot}}|. \quad (26)$$

The projections N^{\parallel} and N^{\perp} to the direction parallel and

perpendicular to the CH_3 top axis, respectively, are calculated as follows:

$$\begin{aligned} |\mathbf{L}_{\text{CH}_3}^{\parallel}| &= N^{\parallel}, & |\mathbf{L}_{\text{CH}_3}^{\perp}| &= N^{\perp}, \\ N^2 &= N^{\parallel 2} + N^{\perp 2}, \end{aligned} \quad (27)$$

IV. RESULTS

A. Features of the potential energy surfaces

At first we describe the global features of the present analytically fitted PES's. We also compare these with the empirical SB and GS surfaces.^{17,35}

Figure 4 shows the present analytical 3Q_0 and 1Q_1 potential energy surfaces for the C_{3v} symmetry. In the C_{3v} symmetry, all the off-diagonal elements V_{ij} are zero, and V_i represents the adiabatic potential surfaces. Figure 4(a) represents the potential energy curves with respect to R with α optimized for each R (cf. Fig. 2). The 1Q_1 curves (degenerate due to the C_{3v} symmetry) monotonically decrease in energy as R increases. On the other hand, 3Q_0 has a shallow well (0.223 eV at $R = 3.493 \text{ \AA}$ and $\alpha = 91.4^\circ$) outside the conical intersection. This is similar to the other *ab initio* result (0.157 eV at $R = 3.5 \text{ \AA}$ and $\alpha = 92.6^\circ$) by Tadjeddine *et al.*²² Brus and Bondybey have pointed out from the analysis of the emission spectrum in the photolysis of CH_3I and CD_3I in Ne at 4.2 K that the 3Q_0 surface is slightly bound ($< 0.248 \text{ eV}$ at $\sim R = 3.3 \text{ \AA}$).⁶

Next we describe the contour maps in the C_{3v} symmetry. As far as the symmetry of the CH_3I system is restricted to C_{3v} , this is exactly equivalent to a linear XCI system,

where X is a pseudoatom placed at the center of mass of three hydrogen atoms with their combined mass. We define a new coordinate system $(R_{\text{tr}}, r_{\text{int}})$, replacing the original coordinate system (R, α) . R_{tr} is the distance between the I atom and the CH_3 center of mass and r_{int} is the XC distance:

$$\begin{aligned} R_{\text{tr}} &= R - (m_X/m_{\text{CX}})r_e \cos \alpha, \\ r_{\text{int}} &= -r_e \cos \alpha. \end{aligned} \quad (28)$$

In this new coordinate system, the kinetic energy operator is diagonal and the internal CX motion, which contributes to the ν_2 mode excitation, is separated from the translational motion, as shown in Eq. (29)

$$\begin{aligned} T &= (1/2)(m_{\text{CX}}m_{\text{I}}/M)\dot{R}_{\text{tr}}^2 + (1/2)(m_{\text{C}}m_X/m_{\text{CX}})\dot{r}_{\text{int}}^2, \\ M &= m_{\text{I}} + m_{\text{C}} + m_X. \end{aligned} \quad (29)$$

Figures 4(b) and 4(c) show the contour maps in the new coordinate system, scaled with the proper mass so that the dynamics on these surfaces can be treated as that of a rolling ball. The reaction coordinate (RC), determined by connecting the minima with respect to r_{int} for each R_{tr} on 3Q_0 , intersects with 1Q_1 at $R_{\text{tr}} = 2.422 \text{ \AA}$, $r_{\text{int}} = 0.2674 \text{ \AA}$, i.e., $R = 2.365 \text{ \AA}$ and $\alpha = 104.3^\circ$. When a point is located on the right- (left-) hand side of the RC, it receives a force which tends to reduce (increase) r_{int} , i.e., α . The change of r_{int} and α on the RC is slow with respect to the change of R_{tr} . Since the Franck-Condon region ($\alpha = 111.2^\circ$) is located slightly away from the RC ($\alpha = 106.0^\circ$ at the same R_{tr}), a small

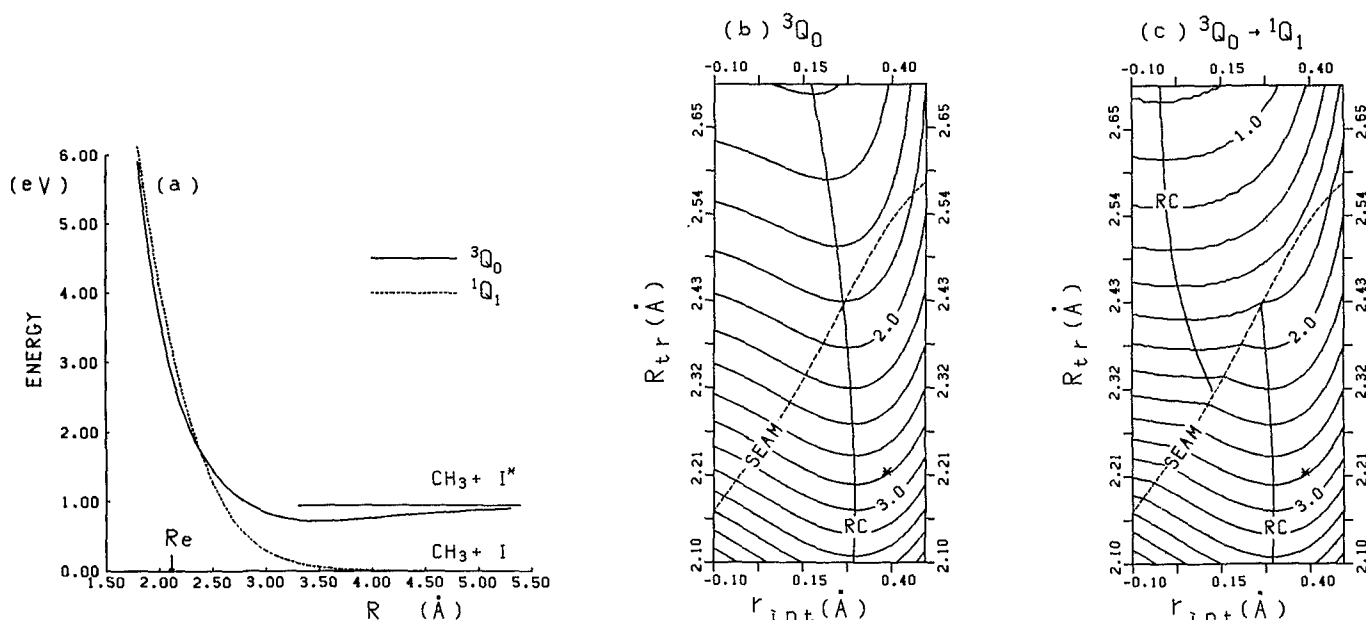


FIG. 4. Present potential energy surfaces in the C_{3v} symmetry. (a) The potential energy curves with respect to R , with α optimized for each R . (b) 3Q_0 and (c) $^3Q_0 \rightarrow ^1Q_1$ contour maps. Contour spacing is 0.2 eV, relative to the $\text{CH}_3 + \text{I}(^2P_{3/2})$ limit. The seam represents the conical intersection, at which 3Q_0 and 1Q_1 surfaces are connected in (c). RC and * represent the reaction coordinate and the ground state equilibrium geometry, respectively.

force for internal excitation is expected in the early stage of reaction on 3Q_0 . In Fig. 4(c), which shows the potential surface 3Q_0 before and 1Q_1 after the seam of conical intersection, one can see that the RC on 1Q_1 has a small r_{int} , i.e., $\alpha \sim 90^\circ$ and is quite far away from RC on 3Q_0 . When a trajectory hops from 3Q_0 to 1Q_1 , the force and the force constant with respect to r_{int} change very much. As will be discussed later, these characteristic differences between 3Q_0 and 1Q_1 are the essential factor governing the difference in ν_2 vibrational excitation in the CH_3 product.

Here we would like to make a brief comparison between the present *ab initio* surfaces in the C_{3v} symmetry and the SB

and GS empirical surfaces (which are defined only within the C_{3v} symmetry) shown in Fig. 5. Both SB and GS 3Q_0 surfaces monotonically decrease without a well, in contrast to the present surface which has a shallow well. The reaction coordinate on both SB 3Q_0 and 1Q_1 surfaces pass through near $r_{\text{int}} = 0$ for any R_{tr} , indicating that as soon as the system is excited to 3Q_0 , CH_3 wants to be planar. The preference of the planar CH_3 does not change by switching from 3Q_0 to 1Q_1 . These imply that the umbrella mode excitation is mainly determined at the Franck-Condon region and that there should be little, if any, channel selectivity.¹⁷ These features are again in clear contrast to those of the present sur-

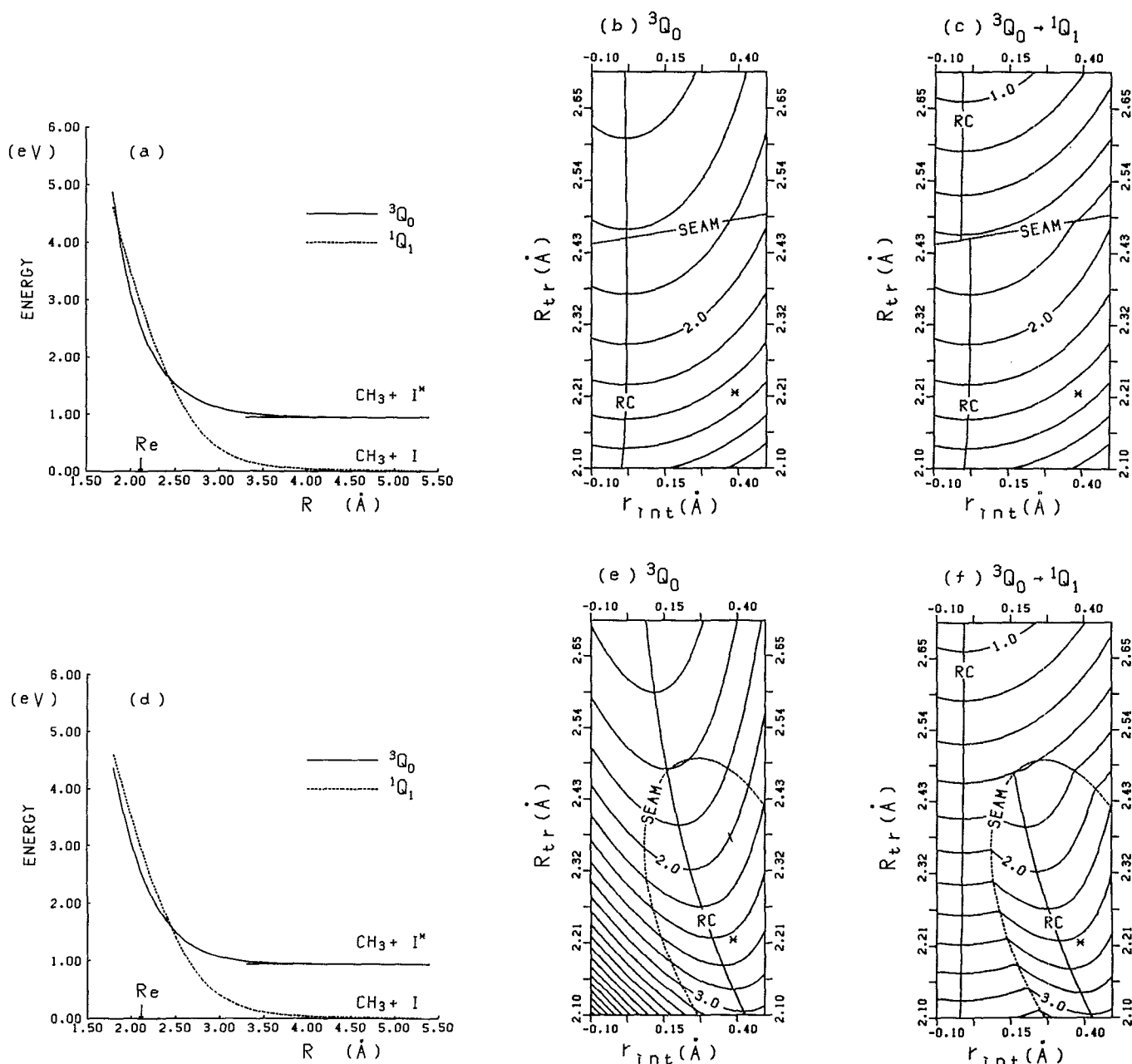


FIG. 5. Empirical potential energy surfaces (a)–(c) by Shapiro and Bersohn, and (d)–(f) by Guo and Schatz. The scale and other glossaries are the same as in Fig. 4.

faces. On the other hand, roughly speaking, the GS surfaces were designed to reproduce the recent experimental findings about the CH_3 ν_2 mode excitation, and are similar to the present surfaces except for the behavior of the conical intersection to be discussed later.³⁵

Figure 6 shows examples of the present potential energy curves with respect to the bending angle θ for a few fixed values of R , where α is optimized for each state. In the Franck-Condon region [see Fig. 6(a)], the 3Q_0 surface has a minimum at $\theta = 0$, whereas the 1Q_1 surface has minima at $\theta = \pm 4^\circ$. This deviation from the C_{3v} symmetry is due to the Jahn-Teller distortion.

Figure 6(b) shows the curves at the conical intersection, where the reaction coordinate of 3Q_0 crosses the 1Q_1 surface. Each adiabatic surface has a minimum at $\theta \neq 0$. When α was fixed at 111.2° , the two surfaces intersect at $R = 2.445 \text{ \AA}$ for $\theta = 0$ and the largest bending angle and the bending stabilization energy were $\theta_{\min} = 6.0^\circ$ and $\Delta E(\theta_{\min}) = E(\theta_{\min}) - E(0^\circ) = -4.3 \times 10^{-3} \text{ eV}$ for the A' state.⁴⁷ When α is allowed to change, the RC of the 3Q_0 surface intersects the 1Q_1 surface at $R = 2.365 \text{ \AA}$ and $\alpha = 104.3^\circ$ for $\theta = 0$ and the largest bending stabilization is $\Delta E(\theta_{\min} = 5.0^\circ) = -5.3 \times 10^{-3} \text{ eV}$; when α is allowed to relax, two surfaces cross at a smaller R . Figure 6(c) shows cuts of PES's outside the conical intersection region. While the 3Q_0 surface has a substantial force constant at $\theta = 0$, the 1Q_1 surfaces are very flat with respect to θ . This difference in the θ dependence between the 1Q_1 and 3Q_0 surfaces, as will be discussed in the next section, is the most important factor determining the energy partitioning into the CH_3 rotation.

B. Rotational excitation

One of the largest concerns in the present study is the distribution of the rotational quantum number in the CH_3 product in each channel. Figure 7 shows the rotational distribution obtained in the trajectory calculation. We can clearly see the channel selectivity. We have found that the rotational angular momentum is nearly perpendicular to the top axis in most trajectories, i.e., $N \approx N^\perp$. Therefore, we use only the total rotational angular momentum N in the following discussion: Qualitatively, the CH_3 product in the I^* channel is rotationally cool, which agrees with recent experiments^{23,25,26} as well as our previous discussion.³⁶ Quantitatively, the present calculation predicts the peak in the rotational distribution at $N = 1$. It is not clear at this point whether this slightly hot distribution is credible or not, considering the fact that the calculation has been carried out by quasiclassical trajectories with zero-point energies. On the other hand, one finds that the product in the I channel is rotationally excited up to $N = 8$ with a peak at $N = 5$. This is in good agreement with the experiment by Chandler and co-workers,²⁶ but is in the quantitative sense in disagreement with the PB experiment that CD_3 is rotationally excited up to $N = 14$. If one accepts the comment that the PB experiment carried out at the room temperature may possibly involve rotationally excited parent molecules which would give hotter laboratory rotational distribution of the product due to poor alignment,^{24,26} the agreement with the experiments is excellent.

We have examined the origin of this selectivity in detail. Figure 8 shows plots of the CH_3 -I distance R_{tr} vs the rota-

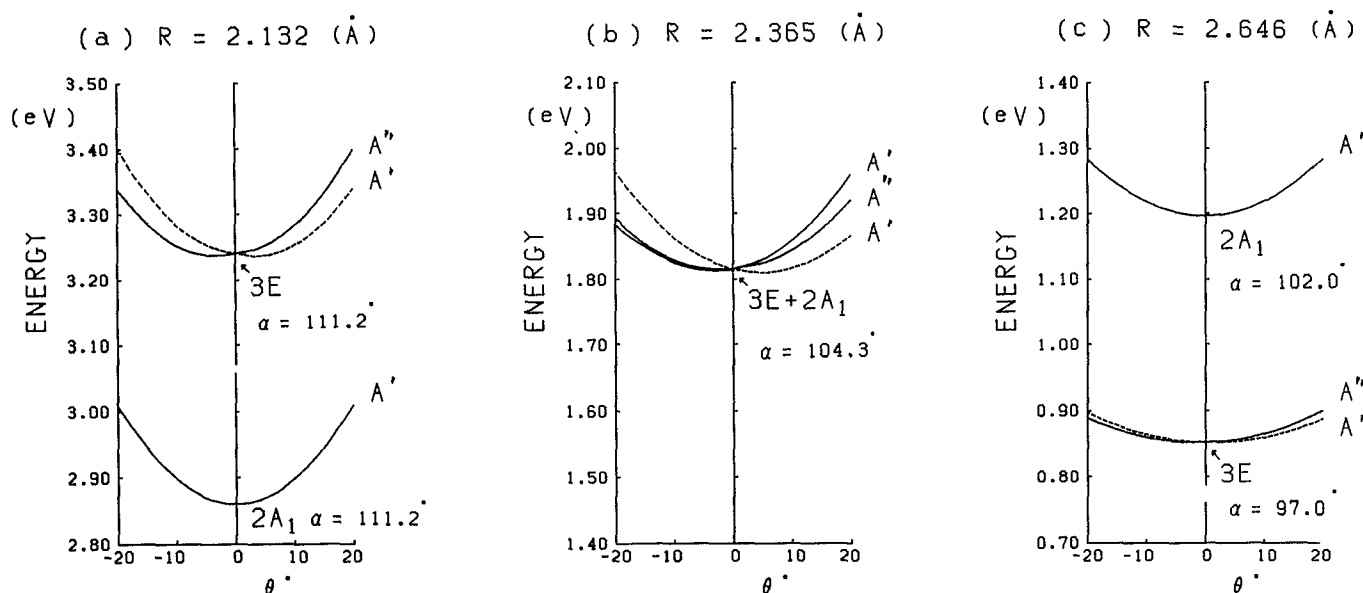


FIG. 6. Adiabatic potential energy curves with respect to θ at (a) the Franck-Condon region, $R = 2.132 \text{ \AA}$; (b) the conical intersection, where the 3Q_0 reaction coordinate crosses 1Q_1 , $R = 2.365 \text{ \AA}$; and (c) outside the conical intersection, $R = 2.646 \text{ \AA}$. The local C_{3v} symmetry of CH_3 is assumed. α is optimized at each R for each state for (a) and (c). The positive and negative values of θ in these figures represent $\phi = 0$ and π , respectively.

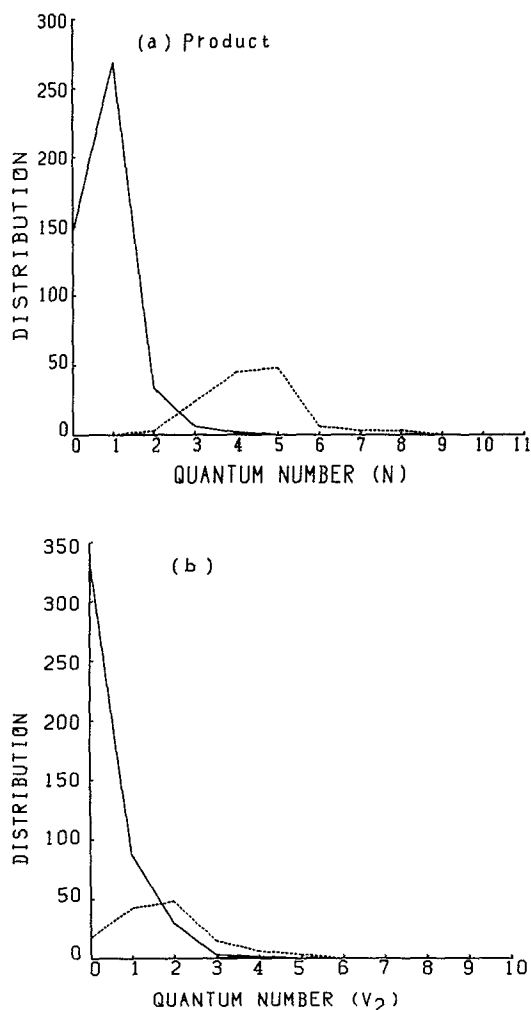


FIG. 7. The final (a) rotational (N) and (b) the umbrella vibrational distribution of the CH_3 product. The reactant CH_3I is in the ground vibrational state. The solid line is the distribution in the I^* channel and the dotted line is the distribution in the I channel, scaled up three times for clarity.

tional energy of the CH_3 fragment and θ for a selected trajectory, which was forced to run on three separate branches. The rotational energy and quantum number of the CH_3 fragment during the reaction was calculated from the atomic velocities, assuming that the CH_3 fragment was completely isolated from I . It can be seen in Fig. 8(a) that the rotation is highly excited ($N = 5$ in this case) *before* the nonadiabatic transition and furthermore the final rotational energy in each channel is determined by whether this excitation is more or less retained (as in the I channel) or is nearly completely damped (as in the I^* channel). In Fig. 8(b), the trajectory on the 1Q_1 surface shows a smooth increase in θ , while the trajectory on 3Q_0 does not. These differences are justifiable in relation to the shape of PES with respect to θ . The 1Q_1 surfaces are very flat even right after the transition region, as shown at $R = 2.646 \text{ \AA}$ in Fig. 6(c). Therefore, the trajectory with the kinetic energy in the "rotational" mode is expected to show a smooth increase in θ , retaining the energy. The 3Q_0 surface, on the other hand, now has a substantial

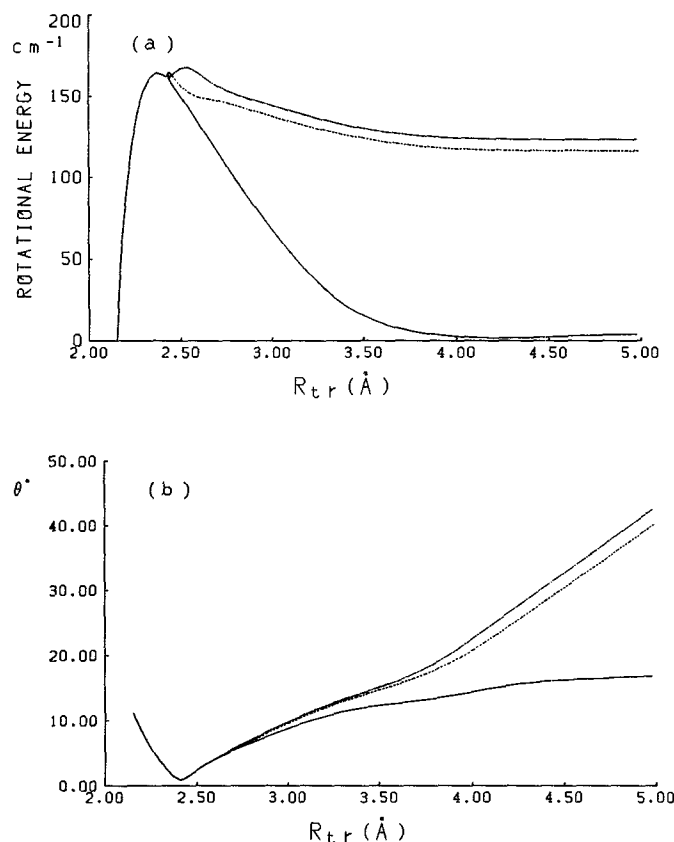


FIG. 8. Plots of R_{tr} vs the rotational energy of the CH_3 fragment and (b) R_{tr} vs θ for a randomly selected trajectory. The solid line represents a trajectory which stayed on the 3Q_0 diabatic state and has given I^* . The dotted and dashed lines are the same trajectory, but have been forced to switch to the $^1Q_1(A')$ and $^1Q_1(A'')$ surfaces, respectively, and to give I .

positive bending force constant around $\theta = 0$, and the trajectory is forced to remain within a small value of θ , releasing the rotational energy into the translational motion. Though Fig. 8 represents one trajectory, this observation is borne out statistically in Fig. 9. The rotational distribution at the transition region (where the decision of making transition or not is made) in Fig. 9(a) shows that CH_3I going to the I^* channel has almost as high a CH_3 rotational quantum number as that going to the I channel. Figure 9(c) shows that the rotational distribution in the I^* channel at $R = 3.704 \text{ \AA}$ has substantially cooled down. On the other hand, the rotational excitation in the I channel remains unchanged (or slightly enhanced) after the transition region. Therefore, we can conclude that the rotational energy is accumulated *before* the transition, and the channel selectivity takes place *after* the transition and is due to the difference in the force constant for bending angle θ outside the conical intersection.

The next question to ask then will be why the rotational distribution at the transition region is hot, as was seen in Fig. 9(a). Here one should recall that as CH_3I travels from the equilibrium geometry ($R_e \sim 2.1 \text{ \AA}$) to the conical intersection region ($R \sim 2.4 \text{ \AA}$), the potential energy of about 1.1 eV

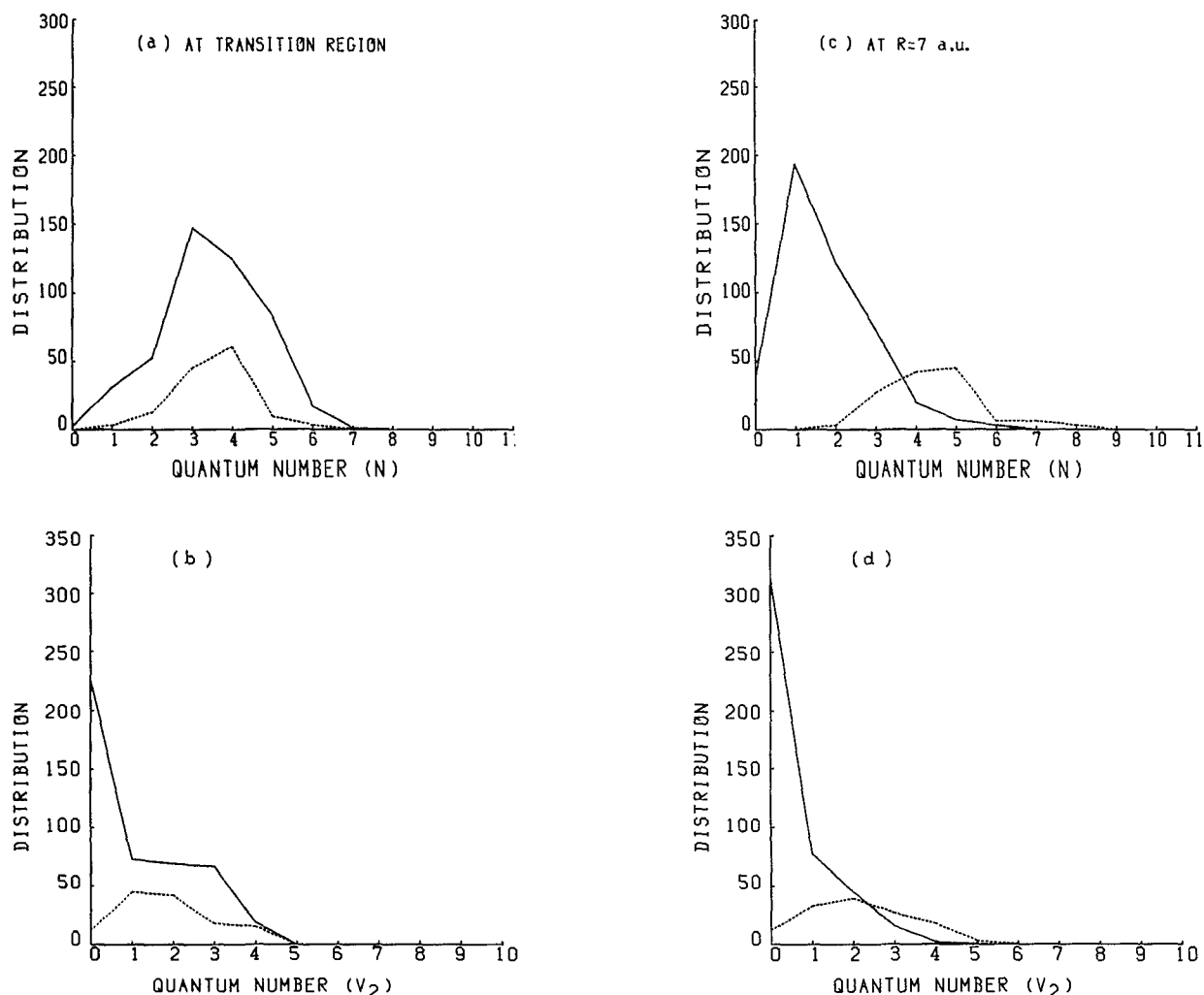


FIG. 9. The rotational (N) and umbrella vibrational (v_2) distribution of the CH_3 fragment during the reaction, (a) and (b) at the transition region, and (c) and (d) at the intermediate region $R = 3.704 \text{ \AA}$. The reactant CH_3I is in the ground vibrational state. Glossaries and scales are the same as in Fig. 7.

is released into the kinetic energy with respect to the $\text{CH}_3\text{--I}$ distance R_{tr} . It is very natural that a small fraction of it (up to 200 cm^{-1} or about 2.2%) shows up in the bending or rotational mode, which is coupled in the dynamics with the $\text{CH}_3\text{--I}$ distance via the zero point vibration of the parent CH_3I molecule. Figure 8(a) actually shows that the buildup of energy in the rotational mode occurs throughout the initial stage of reaction, i.e., the evolution of the system on the 3Q_0 surface.

It is interesting to compare the results of classical trajectory calculation with the impact or sudden model, which we used in our previous paper³⁶ to explain in part the hot CH_3 rotational distribution in the I channel. In this model, trajectories which have a larger θ at the transition region will have more chance to make a transition to the 1Q_1 surface due to the θ dependency of V_{13} and V_{23} . Here the torque due to the energy lowering for the bending $|\Delta E(\theta_{\text{min}})|$ will be converted suddenly into the rotational motion. Trajectories with a small θ , on the other hand, will tend to stay on the 3Q_0 surface and reach the product with unexcited rotation. Figure

10 shows that there might be a weak relation between the final CH_3 rotational quantum number N and the bending angle θ , at which the decision of making a transition or not has been made. We have also found that the final CH_3 rotational quantum number N is unrelated to $\Delta E(\theta_{\text{min}})$ at the point of transition. Because of these results as well as the dynamical details discussed above, one has to conclude that there is no justification of a simple impact model.

C. Relationship between dynamics and crossing point

The crossing between the two electronic states 3Q_0 and 1Q_1 has a close connection to the polarized emission spectroscopy of the dissociating CH_3I molecule by Lao *et al.*³⁴ In their classical, one-dimensional interpretation, the difference in energy between these excited states and the ground state at the crossing R_x , $\Delta E_x = E_{\text{ex}}(R_x) - E_{\text{gr}}(R_x)$, is reflected into the energy dependence of the polarization of emission. When the energy of emitted photon is larger than

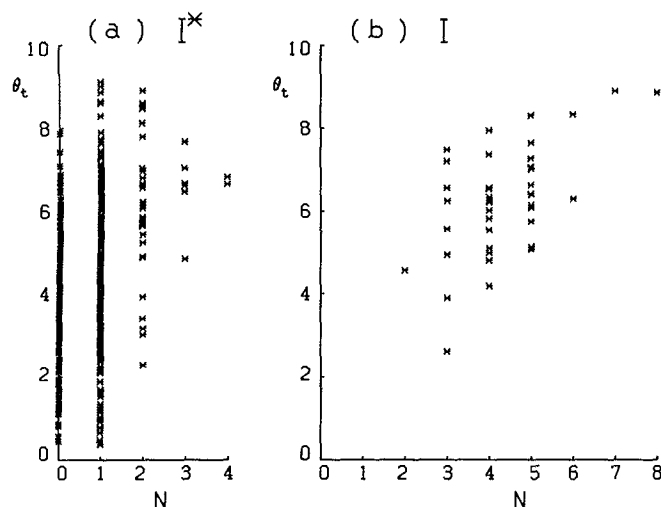


FIG. 10. The bending angle θ_t , at which the decision of making a transition or not has been made, vs the final CH_3 rotational angular momentum N for individual trajectories in (a) the I^* channel and (b) the I channel.

ΔE_x , its polarization is parallel, indicating that the emission takes place from the 3Q_0 surface *before* the CH_3I molecule reaches the crossing. When the photon energy is smaller than ΔE_x , i.e., *after* the crossing is passed, some emission with a perpendicular polarization from the 1Q_1 surface, as well as the parallel transition, appears. The abrupt change in polarization between the emission to the ν_3 (C–I stretch) = 8 level and to the ν_3 = 9 level of the ground state indicates that the excited–ground energy difference at the crossing ΔE_x is 33 000–33 500 cm^{-1} .

We have calculated R_x and ΔE_x , as shown in Table V, using three different methods. In the first method, denoted the static (R) method, the 3Q_0 reaction coordinate (RC) is determined by connecting the potential minima with respect to r_{int} for various values of the C–I distance R within the C_{3v} symmetry, and R_x is defined to be the C–I distance R at which this RC crosses the 1Q_1 surface. We obtained ΔE_x to be 31 035 cm^{-1} at $R = 2.393 \text{ \AA}$ and $\alpha = 106.6^\circ$. This value is similar to the corresponding values $\Delta E_x = 31\,370$ and

29 598 cm^{-1} of the SB and GS surfaces. It is also similar to the values quoted in Ref. 34, presumably calculated with the method similar to this. These values are lower than the experimental estimate by about 2000 cm^{-1} . Lao *et al.*³⁴ have suggested that the calculated C–I distance at the crossing R_x may be too large and that a smaller R_x should give a larger ΔE_x in better agreement with the experiment. This may well be so, because finding the exact location of crossing of two nearly parallel curves is not easy and that ΔE_x should be very sensitive to the location of crossing.

However, one can argue easily that the above method is not correct. Since the kinetic energy matrix for the (R, r_{int}) coordinate system is not diagonal, the results are coordinate dependent. One has to use the coordinate system which has a diagonal kinetic energy matrix, in order to obtain the coordinate independent reaction coordinate with the above minimization procedure.⁴⁸ The $(R_{\text{tr}}, r_{\text{int}})$ coordinate system [Eq. (28)] satisfies this condition. The crossing, determined with this method, denoted static (R_{tr}), for our surfaces occurs at a smaller $R = 2.365 \text{ \AA}$ and a smaller $\alpha = 104.3^\circ$ with a larger $\Delta E_x = 32\,196 \text{ cm}^{-1}$. This correct static value of ΔE_x is still 1000 cm^{-1} too small in comparison with the experimental estimate. However, we can propose that the dynamic effect can account for this discrepancy. Figure 11 shows the plots of the point $(R_{\text{tr}}, r_{\text{int}})$ where the decision of making a transition or not has been made for trajectories. One can see immediately that most trajectories cross the conical intersection at points where both R_{tr} and r_{int} , and therefore R and α , are smaller than the above point determined statically (where SEAM and RC cross in Fig. 11). Trajectories start at the FC region, which is on the right-hand side of the RC. The force in the region is to reduce r_{int} and cause the trajectories on average to reach the seam of crossing at r_{int} which is smaller than r_{int} on RC (see the next section for the trajectory that starts at the ground state equilibrium geometry). The averaged values in Fig. 11, regardless of whether the transition is made (I channel) or not (I^* channel), are $R_{\text{tr}} = 2.395 \text{ \AA}$, $r_{\text{int}} = 0.234 \text{ \AA}$, i.e., $R = 2.345 \text{ \AA}$, $\alpha = 102.5^\circ$, where ΔE_x is calculated to be 33 051 cm^{-1} , which is larger than the static ΔE_x by about 1000 cm^{-1} . Thus, the dynamically determined ΔE_x is in much better agreement with the experimental estimate.

TABLE V. Location of crossing and the excited–ground energy difference

Potentials	Method	R_x (\AA)	α_x ($^\circ$)	$E_{\text{ex}}(R_x, \alpha_x) - E_{\text{gr}}(R_x, \alpha_x)$ (cm^{-1})
Present	Static (R_{tr})	2.365	104.3	32 196
	Static (R)	(2.393)	(106.6)	(31 035)
	Dynamic	2.345	102.5	33 051
Tadjeddine Shapiro	*	2.353	NA	31 100
	Static (R_{tr})	2.413	91.2	31 941
	Static (R)	(2.396)	(97.9)	(31 370)
	*	2.403	NA	30 716
Guo and Schatz	Static (R_{tr})	2.435	98.5	30 136
	Static (R)	(2.440)	(101.1)	(29 598)

* Taken from Table II of Ref. 34. Presumably the method used is static (R).

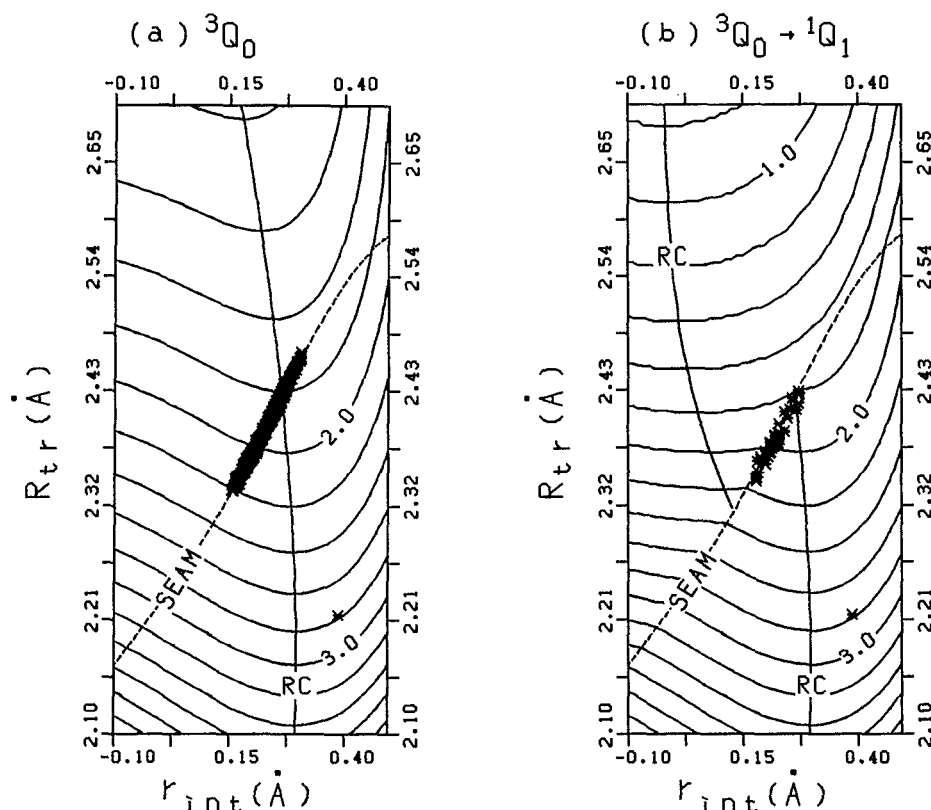


FIG. 11. Plots of R_{tr} vs r_{int} for trajectories at the point where the decision of making the transition or not has been made (a) for the I^* channel and (b) for the I channel, superimposed on the contour maps of Fig. 4.

D. Vibrational excitation of umbrella mode

Now we turn to another important question of the final vibrational distribution in the ν_2 umbrella mode for each channel product. Figure 7(b) gives the results of the trajectory calculation. The distribution in the I -channel product has peak at $\nu = 2$ and this propensity is in good agreement with experimental results.²⁸ On the other hand, the I^* -channel product is vibrationally cold. This is also in good agreement with recent experiments by Houston and co-workers,^{23,26} and Suzuki *et al.*³⁰ who observed in the I^* channel that the cold ($\nu_2 = 0$) product is more abundant than the vibrationally hot ($\nu_2 = 2$) product.

We have examined the reason why the CH_3 vibrational distribution is different between the I and the I^* channels. For this purpose, we use a trajectory that starts exactly at the ground state equilibrium geometry without initial kinetic energy and travels initially on the 3Q_0 surface. This trajectory maintains the C_{3v} symmetry during its evolution; we treat the dynamics as a linear triatomic XCI system. The trajectory was forced to run in two branches, with or without making $^3Q_0 \rightarrow ^1Q_1$ transition at the conical intersection. Figure 12 shows energetics and Fig. 13 actual traces of two branches of the trajectory. As shown in Fig. 12(a), most of the potential energy released during the dissociation is converted into the kinetic energy of the CH_3 center of mass as well as that of the I atom (not shown). The difference in the

kinetic energy between the two channels reflects the difference in the electronic energy between I and I^* . Figure 12(b) shows the plots of R_{tr} vs the internal kinetic energy contributing to the ν_2 mode, which is equal to the second term in Eq. (29). There are two questions to be answered in this figure. The first is why the internal kinetic energy decreases slightly just before the transition. As shown in Fig. 13(a) and discussed in Sec. IV A, the starting point of the trajectory is on the right-hand side of the RC on the 3Q_0 surface, and the force acting on it has a strong component to shorten r_{int} , as shown in Fig. 13(a) (as well as the much larger component to stretch R_{tr} which is not shown), and causes the trajectory to travel to the left, crossing the RC, with an increased kinetic energy in the r_{int} mode. However, as the trajectory evolves in time, the internal force changes the sign, causing the internal kinetic energy to decrease. The second question is the origin of the difference between the I and I^* channels after the conical intersection. Two branches of the trajectory for I^* and I , shown in Figs. 13(a) and 13(b), respectively, clearly demonstrate what is happening. When the trajectory in Fig. 13(b) crosses the seam onto 1Q_1 , the force with respect to r_{int} changes the sign abruptly, and the kinetic energy in the r_{int} motion increases rapidly [Fig. 12(b)]. The potential energy in the r_{int} motion, defined as the energy relative to the minimum with respect to r_{int} , of course changes discontinuously at the seam upon going into the I channel, as seen in

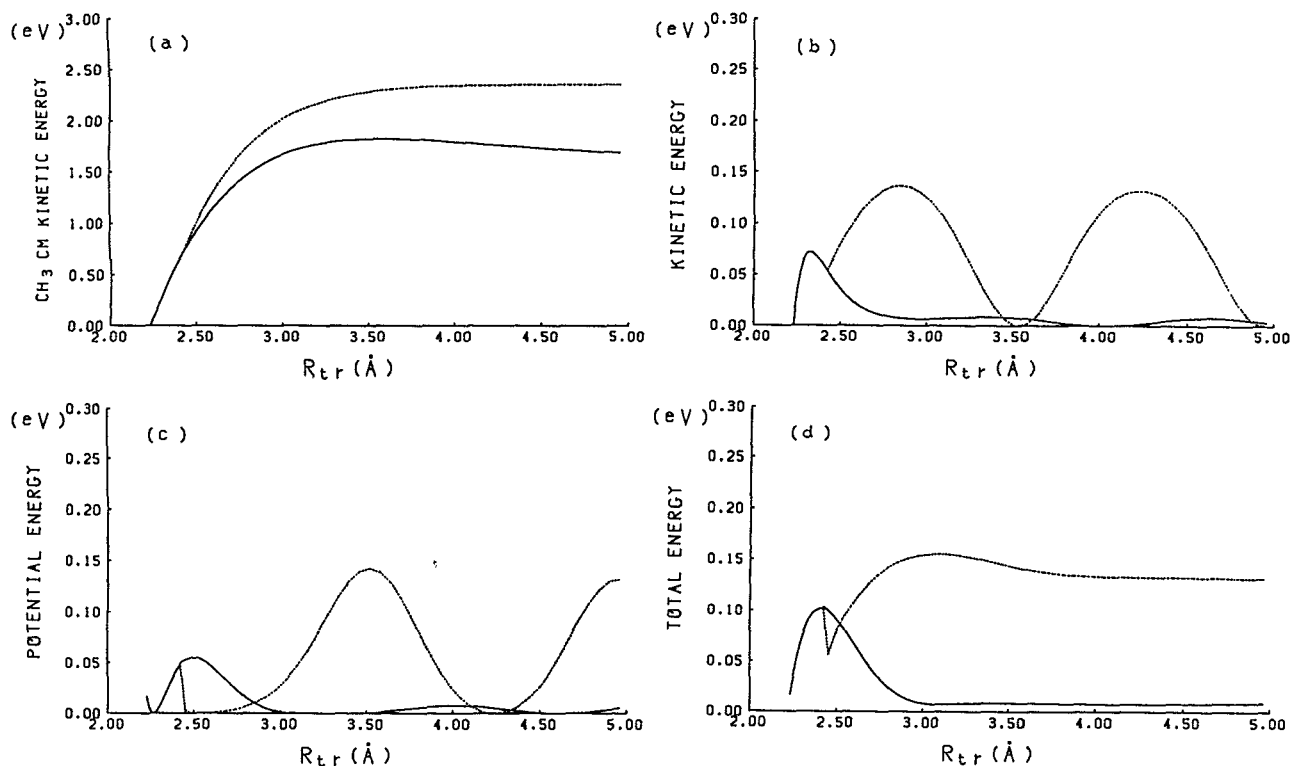


FIG. 12. Plots of R_{tr} vs (a) the kinetic energy of the CH_3 center of mass; (b) the kinetic K ; (c) the potential V ; and (d) the total energy ($K + V$) in the "umbrella" mode, for the trajectory that starts at the ground state equilibrium geometry without initial kinetic energy. The solid and dotted lines represent the branches giving I^* and I , respectively.

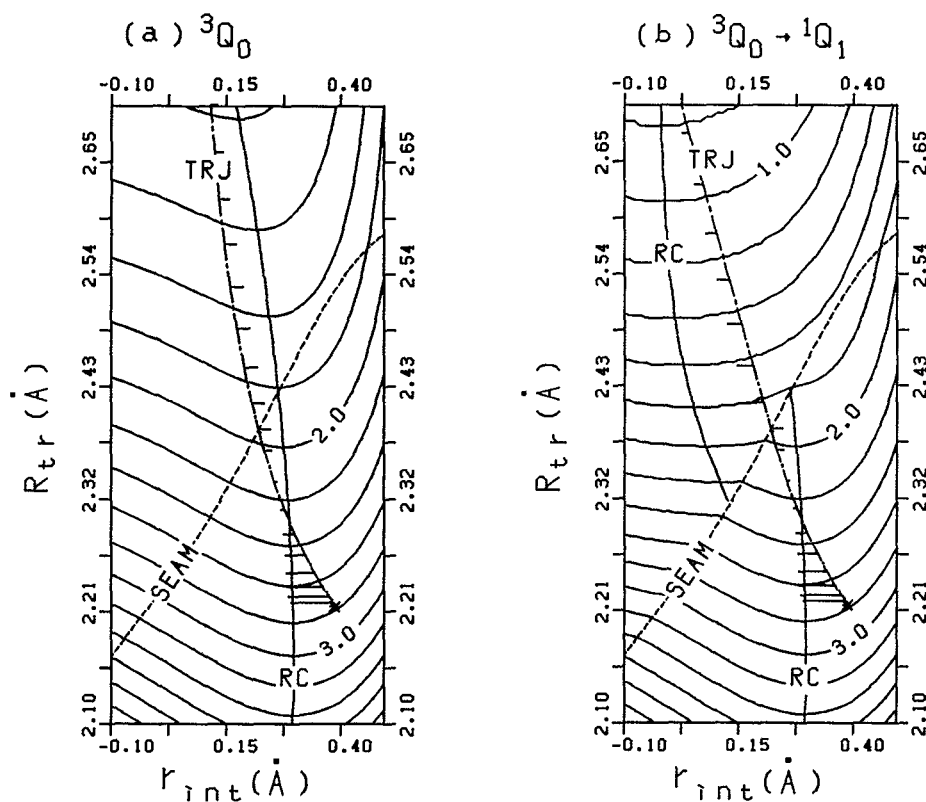


FIG. 13. Plots of the zero-energy pseudolinear trajectory (denoted TRJ), superimposed on the contour map, for (a) I^* -channel product and (b) I -channel product. The internal force $\delta V / \delta r_{int}$ is also shown, in an arbitrary scale for several values of R_{tr} in the figure.

Fig. 12(c), because the optimal r_{int} differs very much between 3Q_0 and 1Q_1 . The total energy in this r_{int} motion, i.e., the ν_2 mode, calculated as the sum of the kinetic and potential energies in Fig. 12(d), increases by $R_{\text{tr}} = 2.8 \text{ \AA}$ up to 0.15 eV, at which level the ν_2 vibration is maintained into the product. On the other hand, for the trajectory remaining on the 3Q_0 surface [Fig. 13(a)], the force is maintained not to decrease r_{int} rapidly and therefore the vibrational energy which had been accumulated up to the conical intersection is depleted rapidly. This dramatic difference between the two channels essentially comes from the difference in the RC, i.e., the difference in the optimal r_{int} on the two surfaces; the 3Q_0 surface has a relatively large r_{int} , therefore a large α , for instance, $r_{\text{int}} = 0.26 \text{ \AA}$, $\alpha = 103.9^\circ$ at $R_{\text{tr}} = 2.45 \text{ \AA}$ and $r_{\text{int}} = 0.13 \text{ \AA}$, $\alpha = 96.9^\circ$ at $R_{\text{tr}} = 2.80 \text{ \AA}$, whereas the 1Q_1 surface has nearly $r_{\text{int}} = 0$, $\alpha = 90^\circ$ for any R_{tr} after the conical intersection.

This analysis of the zero-energy quasilinear trajectory is actually statistically borne out in the full-dimensional trajectory calculation. As was shown in Fig. 9(b) at the transition region, both I- and I*-channel products are still cool. However, at the intermediate region ($R = 3.704 \text{ \AA}$) [Fig. 9(d)], the I-channel product becomes hot and its population is close to that of the final state [Fig. 7(b)]. On the other hand, the I*-channel product is cooler in the intermediate region than at the transition region. From the above discussions, we conclude that the difference in the ν_2 mode excitation between the two channels is due to the difference in the shape of PES; 1Q_1 wants to have a planar CH_3 , whereas 3Q_0 wants to maintain the bent structure until $\text{CH}_3\text{--I}$ distance becomes very large.

We can briefly point out why the SB potential surfaces give an inverted population in the I* channel as well as in the I channel. As discussed in Sec. IV A, the SB 3Q_0 surface, as well as the 1Q_1 surface, has the optimal $r_{\text{int}} \approx 0$ for any R_{tr} . The excitation of the CH_3 umbrella motion takes place immediately upon excitation to the 3Q_0 surface, and the $^3Q_0 \rightarrow ^1Q_1$ hop makes very little difference in the dynamics. These defects of the SB surfaces disappear in the GS surfaces, which make it possible to have a discussion similar to the present one. As shown in Figs. 5(e) and 5(f), however, the behavior of the conical intersection of the GS surfaces is very different from that of the present surfaces. The GS surfaces have such a skewed conical intersection seam that some trajectories may actually cross the seam near the FC region.

E. The effect of initial conditions—mode selectivity

In order to assess how the initial vibrational states of CH_3I in the ground electronic state affect the dynamics, we have carried out additional trajectory calculations with an initial excitation by one quantum number in each of the vibrational modes ν_2 , ν_3 , ν_5 , and ν_6 of CH_3I . The product distributions of the ν_2 vibrational and the rotational quantum numbers thus obtained are shown in Fig. 14. These figures should be directly compared with Fig. 7, which is for the initial ground vibrational state of CH_3I . The excitation in the ν_3 C–I stretching mode has no effect on the product

internal energy distribution. This is understandable because this C–I mode becomes the dissociation mode in the excited state. The excitation in the ν_2 CH_3 umbrella mode gives a higher excitation in the ν_2 mode in the CH_3 product for both I and I* channels, but makes very little difference in the rotational distribution. Of course, the ν_2 mode of CH_3I is directly correlated to the ν_2 mode of CH_3 . The excitation in the ν_6 rocking mode, which is correlated to the CH_3 rotation, gives a substantially higher rotational excitation in both I and I* channels. This mode also gives a higher I/I* branching ratio. The ν_6 mode destroys the C_{3v} symmetry of the system due to varying θ and promotes a coupling (which is zero in the C_{3v} symmetry) and therefore increases a transfer between diabatic surfaces. The ν_5 mode also destroys the C_{3v} symmetry due to changing β_i 's. However, the branching ratio (as well as the distributions) is little influenced by the ν_5 mode excitation. This is understandable because the β_i 's part in the coupling elements V_{13} and V_{23} is a quarter or less of the θ part. All these results indicate that the internal energy given to a particular mode of the reactant remains there substantially and is converted rather adiabatically into the energy of the product. This is understandable considering the fact that the time required for photodissociation (about 10 fs up to the transition region and about 20 fs to reach at $R = 3.0 \text{ \AA}$) is shorter or of the same order to the period of vibrational motions (about 20–60 fs). The dissociation occurs too fast for the internal energy to redistribute.

In the PB experiment which may be using rotationally warm CH_3I molecules, a possibility of contribution of vibrationally excited CH_3I can also be suggested. About 1.5% of CH_3I molecules in room temperature is excited to the $v = 1$ excited state of the ν_6 vibrational mode, which would give a contribution to highly rotationally excited CH_3 product in the I channel, as is seen in Fig. 14(g).

F. Branching ratio

Several experimentalists have reported that the $\text{I}^*/(\text{I} + \text{I}^*)$ branching ratio of photolysis at 266 nm ranging from 0.6 to 0.9, most frequently about 0.7.^{4,5,7–12} The branching ratio in our trajectory calculation 0.91 is significantly larger than 0.7. In the present model, the branching ratio is determined by V_{13} or V_{23} according to Eq. (24), and they are functions of the bending angle θ and the degenerate CH_3 deformation as shown in Eqs. (17) and (18). Equations (17) and (18) are valid, as far as only six degrees of freedom are used in the potential functions and consequently in the dynamics. If three C–H stretching degrees of freedom, frozen in the present study, are taken explicitly into account, however, the degenerate stretching modes $S_{4a} = 1/\sqrt{6}(2\Delta r_1 - \Delta r_2 - \Delta r_3)$ and $S_{4b} = 1/\sqrt{2}(\Delta r_2 - \Delta r_3)$ are expected to contribute to V_{13} and V_{23} as well. Our preliminary *ab initio* SOCI calculations with varying C–H distances⁴⁹ indicate that actually there are new additive contributions from S_{4a} and S_{4b} of the same order of magnitude as the terms in Eqs. (17) and (18). Thus, if we carry out a trajectory calculation using potential functions including C–H stretches, the branching ratio is expected to decrease, to approach experimental values. A recent experimental find-

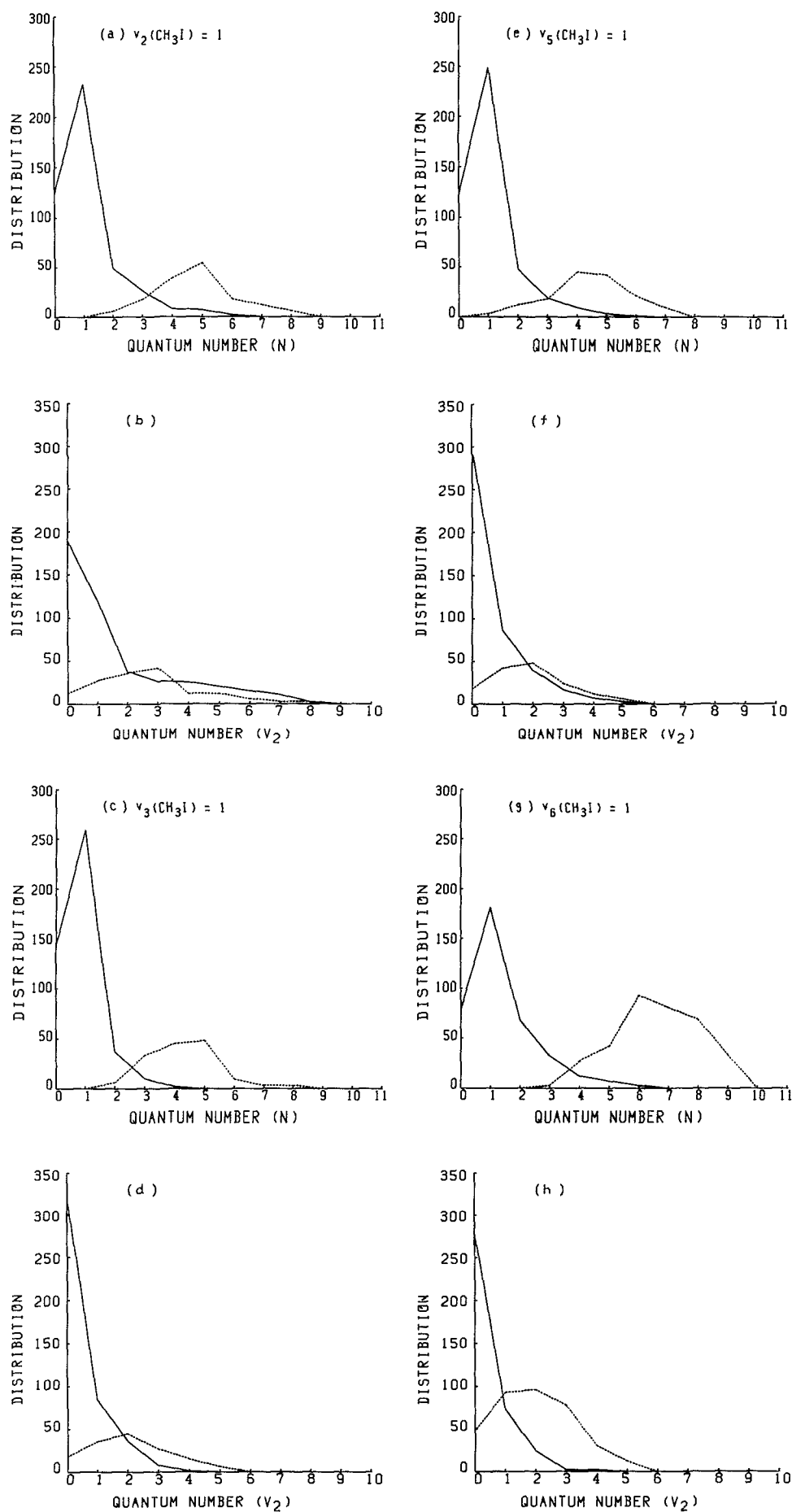


FIG. 14. The final rotational (N) and umbrella vibrational (v_2) distribution of CH_3 product. The initial vibrational state of the parent molecule CH_3I is excited by one quantum of (a), (b) v_1 : sym- CH_3 -def.; (c), (d) v_3 : C-I str.; (e), (f) v_5 : d - CH_3 -def.; the (g) and (h) v_6 : d - CH_3 -rock. Glossaries and scales are the same as in Fig. 7.

ing shows that the symmetric C–H stretch ν_1 of the CH_3 product takes place preferentially in the I channel.³⁰ This could be just a matter of difference in the exothermicity, but could also imply the importance of C–H stretch in the dynamics.

In the present model, trajectories are restricted to start on 3Q_0 , based on the experimental fact that 94% of the absorption is $^3Q_0 \leftarrow ^1A_1$ at about 260 nm.⁴ The experiment also indicates that a few percent of the A-band absorption is $^1Q_1 \leftarrow ^1A_1$. We have also carried out a trajectory calculation starting on the 1Q_1 state. In this case, the branching ratio to the I^* and I channels is calculated to be 0.03:0.97. Therefore, the contribution of a few percent of $^1Q_1 \leftarrow ^1A_1$ absorption is expected to decrease the calculated branching ratio $\text{I}^*/(\text{I} + \text{I}^*)$ by a few percent.

V. CONCLUDING REMARKS

We have calculated the potential energy surfaces of CH_3I photodissociation with the contracted spin-orbit CI method. The contracted SOCI gives the results almost indistinguishable to the uncontracted SOCI method, while reducing the computer time substantially.

Our analytical potential functions, derived from *ab initio* results in six degrees of freedom, and surface hopping trajectories on them can reproduce important recent experimental results, including (i) the hot CH_3 rotational distribution with peak at $N=5$ in the I channel and the cold distribution in the I^* channel; (ii) the hot CH_3 ν_2 vibrational distribution with peak at $\nu_2 = 2$ in the I channel and the cold distribution in the I^* channel; and (iii) the excited-ground energy difference at the seam of conical intersection where trajectories make a transition, if the dynamics effect is taken into account.

The CH_3 rotational excitation is mainly determined by the shape of potential energy surfaces with respect to the bending angle θ outside the conical intersection. The rotation is hot when trajectories arrive at the conical intersection. If a transition is made onto the 1Q_1 surface to give an I-channel product, the 1Q_1 surface which is flat with respect to θ retains the rotational excitation. If the trajectory stays on 3Q_0 to give an I^* -channel product, the 3Q_0 surface which has a large bending force constant damps the rotational excitation. The CH_3 ν_2 vibrational excitation, on the other hand, is mainly determined by the shape of potential surfaces with respect to the CH_3 umbrella angle α outside the conical intersection. The reaction coordinate on 1Q_1 has $\alpha \sim 90^\circ$ outside the conical intersection, whereas that on 3Q_0 retains relatively large $\alpha \sim 110^\circ$, until the CH_3 –I distance is very large. The ν_2 vibration is relatively cool when trajectories arrive at the conical intersection. If a transition is made from 3Q_0 to 1Q_1 to give an I-channel product, the trajectory receives an abrupt, strong force to reduce α , because of the difference in the optimal α between two surfaces, and the ν_2 vibration becomes excited. If the trajectory stays on 3Q_0 , energy cannot easily flow into the vibrational mode.

Trajectories cross the conical intersection on average with a smaller CH_3 –I distance and a smaller CH_3 umbrella angle than what the reaction coordinate indicates. This dy-

namical effect can account for the discrepancy in the ground-excited energy difference between the polarized emission experiment and the calculation on the reaction coordinate.

ACKNOWLEDGMENTS

We would like to acknowledge Dr. Powis, Dr. Houston, Dr. Chandler, Dr. Leone, Dr. Hirota, Dr. Kanamori, and Dr. Suzuki for preprints and valuable discussions. We wish to also thank Dr. K. Yamashita for his comments and discussions. All the numerical calculations were carried out at the IMS Computer Center.

APPENDIX

Considering the numerical behavior of the diabatic terms and the requirement that the adiabatic 3Q_0 and 1Q_1 energies are invariant under permutation among the three hydrogen atoms, the fitting functions have to have the forms shown in Eqs. (A1)–(A6)

$$V_1 = V_{10} + P_1 X + P_2 S_a, \quad (\text{A1})$$

$$V_2 = V_{10} - (P_1 X + P_2 S_a), \quad (\text{A2})$$

$$V_3 = V_{30}, \quad (\text{A3})$$

$$V_{12} = P_1 Y + P_2 S_b, \quad (\text{A4})$$

$$V_{13} = Q_1 X + Q_2 S_a, \quad (\text{A5})$$

$$V_{23} = -(Q_1 Y + Q_2 S_b), \quad (\text{A6})$$

where V_{10} , V_{30} , P_1 , P_2 , Q_1 , and Q_2 are functions with respect to R , α , and θ , which are invariant under permutation, and S_a , S_b , X , and Y are defined by Eqs. (A7)–(A10)

$$S_a = 1/\sqrt{6}(2\Delta\beta_1 - \Delta\beta_2 - \Delta\beta_3), \quad (\text{A7})$$

$$S_b = 1/\sqrt{2}(\Delta\beta_2 - \Delta\beta_3), \quad (\text{A8})$$

$$X(\phi, \beta_2, \beta_3, \xi) = \{\cos(3\phi + \xi) + \cos[3(\phi + \beta_3) + \xi] + \cos[3(\phi - \beta_2) + \xi]\}/3, \quad (\text{A9})$$

$$Y(\phi, \beta_2, \beta_3, \xi) = \{\sin(3\phi + \xi) + \sin[3(\phi + \beta_3) + \xi] + \sin[3(\phi - \beta_2) + \xi]\}/3, \quad (\text{A10})$$

$$\tan \xi = S_b/S_a. \quad (\text{A11})$$

A set of dihedral angles $A = \{\phi, \phi + \beta_3, \phi - \beta_2\}$ are defined by those of the I atom against the three hydrogen atoms H^1 , H^2 , and H^3 , respectively (cf. Fig. 2). If one permutes two hydrogens, one would obtain another set of angles $A' = \{\phi', \phi' + \beta_3', \phi' - \beta_2'\}$. However, two sets A and A' are identical.

Next we comment on the phase factor ξ in X (and Y). The secular equation composed of Eqs. (A1)–(A6) gives a cubic equation in Eq. (A12)

$$\begin{aligned} x^3 - (2V_{10} + V_{30})x^2 + [-(V_{10}^2 + 2V_{10}V_{30}) \\ + (P_1^2 + Q_1^2)(X^2 + Y^2) + (P_1^2 + Q_1^2)(S_a^2 + S_b^2) \\ + (P_1P_2 + Q_1Q_2)(XS_a + YS_b)]x - (V_1V_2V_3 \\ + 2V_{12}V_{23}V_{13} - V_1^2V_{23} - V_2^2V_{13} + V_3^2V_{12}) = 0. \end{aligned} \quad (\text{A12})$$

In order to satisfy the energy invariance under permutation, the coefficients of the cubic equation have to satisfy the invariance under permutation. The coefficients of the second order and the first to third coefficients of the first order are invariant. If one chooses the phase factor ξ determined by Eq. (A11), the fourth coefficient of the first order in Eq. (A12) equals $X(\phi, \beta_2, \beta_3, 0)$, which is invariant due to the fact that the dihedral angle set A is invariant. It can be also proved that the constant term is invariant under permutation.

- ¹ J. V. V. Kasper and G. C. Pimentel, *Appl. Phys. Lett.* **5**, 231 (1964).
- ² M. J. Dzvonik and S. C. Yang, *Rev. Sci. Instrum.* **45**, 750 (1974).
- ³ M. J. Dzvonik, S. C. Yang, and R. Bersohn, *J. Chem. Phys.* **61**, 4408 (1974).
- ⁴ A. Gedanken and M. D. Rowe, *Chem. Phys. Lett.* **34**, 39 (1975).
- ⁵ S. J. Riely and K. R. Wilson, *Faraday Discuss. Chem. Soc.* **53**, 132 (1972).
- ⁶ L. E. Brus and V. E. Bondybey, *J. Chem. Phys.* **65**, 71 (1976).
- ⁷ M. D. Barry and P. A. Gorry, *Mol. Phys.* **52**, 461 (1984).
- ⁸ R. K. Sparks, K. Shobatake, L. R. Carlson, and Y. T. Lee, *J. Chem. Phys.* **75**, 3838 (1981).
- ⁹ S. L. Baughcum and S. R. Leone, *J. Chem. Phys.* **72**, 6531 (1980).
- ¹⁰ G. N. A. van Veen, T. Baller, A. E. de Vries, and N. J. A. van Veen, *Chem. Phys.* **87**, 405 (1984).
- ¹¹ H. W. Hermann and S. R. Leone, *J. Chem. Phys.* **76**, 4766 (1982).
- ¹² W. P. Hess, S. J. Kohler, H. K. Haugen, and S. R. Leone, *J. Chem. Phys.* **84**, 2143 (1986).
- ¹³ J. K. Knee, L. R. Khundkar, and A. H. Zewail, *J. Chem. Phys.* **83**, 1996 (1985).
- ¹⁴ T. F. Hunter and K. S. Kristjansson, *Chem. Phys. Lett.* **58**, 291 (1978).
- ¹⁵ M. Shapiro and R. Bersohn, *Annu. Rev. Phys. Chem.* **33**, 409 (1982).
- ¹⁶ M. Shapiro and R. Bersohn, *J. Chem. Phys.* **72**, 3810 (1980).
- ¹⁷ M. Shapiro, *J. Phys. Chem.* **90**, 3644 (1986).
- ¹⁸ S. Y. Lee and E. J. Heller, *J. Chem. Phys.* **76**, 3035 (1982).
- ¹⁹ S. Kanfer and M. Shapiro, *J. Phys. Chem.* **88**, 3964 (1984).
- ²⁰ R. L. Sundberg, D. Imre, M. O. Hale, J. L. Kinsey, and R. D. Coalson, *J. Phys. Chem.* **90**, 5001 (1986).
- ²¹ S. K. Gray and M. S. Child, *Mol. Phys.* **51**, 189 (1984).
- ²² M. Tadjeddine, J. P. Flament, and C. Teichtel, *Chem. Phys.* **118**, 45 (1987).
- ²³ R. O. Loo, H. P. Haerri, G. E. Hall, and P. L. Houston, *J. Chem. Phys.* **90**, 4222 (1989).
- ²⁴ J. F. Black and I. Powis, *J. Chem. Phys.* **89**, 3986 (1988).
- ²⁵ I. Powis and J. F. Black, *J. Phys. Chem.* **93**, 2461 (1989).
- ²⁶ D. W. Chandler, J. W. Thoman, Jr., M. H. M. Jassen, and D. H. Parker, *Chem. Phys. Lett.* **156**, 151 (1989).
- ²⁷ R. O. Loo, G. E. Hall, H. P. Haerri, and P. L. Houston, *J. Phys. Chem.* **92**, 5 (1988).
- ²⁸ J. F. Black and I. Powis, *Chem. Phys.* **125**, 375 (1988).
- ²⁹ D. W. Chandler and P. L. Houston, *J. Chem. Phys.* **87**, 1445 (1987).
- ³⁰ (a) H. Kanamori and E. Hirota (private communication); (b) T. Suzuki, H. Kanamori, and E. Hirota (private communication).
- ³¹ G. E. Hall, T. J. Sears, and J. M. Frye, *J. Chem. Phys.* **90**, 6234 (1989).
- ³² D. Imre, J. L. Kinsey, A. Asinha, and J. Krenos, *J. Phys. Chem.* **88**, 3956 (1984).
- ³³ M. O. Hale, G. E. Galcica, S. G. Glogover, and J. L. Kinsey, *J. Phys. Chem.* **90**, 4997 (1986).
- ³⁴ K. Q. Lao, M. D. Person, P. Xayariboun, and L. J. Butler, *J. Chem. Phys.* **92**, 823 (1990).
- ³⁵ H. Guo and G. C. Schatz, *J. Chem. Phys.* **93**, 393 (1990).
- ³⁶ S. Yabushita and K. Morokuma, *Chem. Phys. Lett.* **153**, 517 (1988).
- ³⁷ (a) S. Huzinaga, *J. Chem. Phys.* **42**, 1293 (1965); (b) T. H. Dunning, Jr., *ibid.* **53**, 2823 (1970).
- ³⁸ W. R. Wadt and P. J. Hay, *J. Chem. Phys.* **82**, 284 (1985).
- ³⁹ (a) R. Shepard, I. Shavitt, R. M. Pitzer, D. C. Comeau, M. Pepper, H. Lischka, P. G. Szalay, R. Ahlrichs, F. B. Brown, and J.-G. Zhao, *Int. J. Quantum. Chem. Symp.* **22**, 149 (1988); (b) IMS Computer Center Library, implemented by S. Yabushita.
- ⁴⁰ J. S. Cohen, W. R. Wadt, and P. J. Hay, *J. Chem. Phys.* **71**, 2995 (1979).
- ⁴¹ Landolt-Bornstein New Series, edited by K. H. Hellwege (Springer, Berlin, 1976), Vol. 7, p. 42.
- ⁴² V. Spiko and P. R. Bunker, *J. Mol. Spectrosc.* **95**, 381 (1982).
- ⁴³ *Theory of Chemical Reaction Dynamics*, edited by M. Baer (CRC, Boca Raton, 1985), p. 1.
- ⁴⁴ *Tables of Molecular Vibrational Frequencies*, edited by T. Shimanouchi (NSRDS-NBS 39, U.S. GP., Washington D.C., 1972), Vol. 1.
- ⁴⁵ *Theory of Elementary Atomic and Molecular Processes in Gases*, edited by E. E. Nikitin (Clarendon, Oxford, 1974), Chap 3.
- ⁴⁶ R. K. Preston and J. C. Tully, *J. Chem. Phys.* **54**, 4297 (1971).
- ⁴⁷ This is slightly different from our previous result that $\alpha = 111.2^\circ$ (fixed), $R = 2.445 \text{ \AA}$, $\theta_{\min} = 6.4^\circ$, and $\Delta E(\theta_{\min}) = -5.3 \times 10^{-3} \text{ eV}$.
- ⁴⁸ (a) K. Fukui, S. Kato, and H. Fujimoto, *J. Am. Chem. Soc.* **97**, 1 (1975); (b) S. Kato and K. Morokuma, *J. Chem. Phys.* **73**, 3900 (1980).
- ⁴⁹ Y. Amatatsu, S. Yabushita, and K. Morokuma (to be published).